

2015

Clique topology reveals intrinsic geometric structure in neural correlations

Chad Giusti

University of Pennsylvania, cgiusti@seas.upenn.edu

Eva Pastalkova

Howard Hughes Medical Institute, Ashburn, VA


Carina Curto

University of Nebraska-Lincoln, ccurto2@math.unl.edu

Vladimir Itskov

Pennsylvania State University - Main Campus, vladimir.itskov@psu.edu

Follow this and additional works at: <http://digitalcommons.unl.edu/mathfacpub>

 Part of the [Cellular and Molecular Physiology Commons](#), [Geometry and Topology Commons](#), [Molecular and Cellular Neuroscience Commons](#), [Other Applied Mathematics Commons](#), [Other Cell and Developmental Biology Commons](#), [Other Mathematics Commons](#), [Structural Biology Commons](#), and the [Systems Neuroscience Commons](#)

Giusti, Chad; Pastalkova, Eva; Curto, Carina; and Itskov, Vladimir, "Clique topology reveals intrinsic geometric structure in neural correlations" (2015). *Faculty Publications, Department of Mathematics*. 84.
<http://digitalcommons.unl.edu/mathfacpub/84>

This Article is brought to you for free and open access by the Mathematics, Department of at DigitalCommons@University of Nebraska - Lincoln. It has been accepted for inclusion in Faculty Publications, Department of Mathematics by an authorized administrator of DigitalCommons@University of Nebraska - Lincoln.

Clique topology reveals intrinsic geometric structure in neural correlations

Chad Giusti^{a,b}, Eva Pastalkova^c, Carina Curto^{b,d,1}, and Vladimir Itskov^{b,d,1,2}

^aWarren Center for Network and Data Science, Departments of Bioengineering and Mathematics, University of Pennsylvania, Philadelphia, PA 19104; ^bDepartment of Mathematics, University of Nebraska, Lincoln, NE 68588; ^cJanelia Research Campus, Howard Hughes Medical Institute, Ashburn, VA 20147; and ^dDepartment of Mathematics, The Pennsylvania State University, University Park, PA 16802

Edited by William Bialek, Princeton University, Princeton, NJ, and approved September 23, 2015 (received for review April 28, 2015)

Detecting meaningful structure in neural activity and connectivity data is challenging in the presence of hidden nonlinearities, where traditional eigenvalue-based methods may be misleading. We introduce a novel approach to matrix analysis, called clique topology, that extracts features of the data invariant under nonlinear monotone transformations. These features can be used to detect both random and geometric structure, and depend only on the relative ordering of matrix entries. We then analyzed the activity of pyramidal neurons in rat hippocampus, recorded while the animal was exploring a 2D environment, and confirmed that our method is able to detect geometric organization using only the intrinsic pattern of neural correlations. Remarkably, we found similar results during nonspatial behaviors such as wheel running and rapid eye movement (REM) sleep. This suggests that the geometric structure of correlations is shaped by the underlying hippocampal circuits and is not merely a consequence of position coding. We propose that clique topology is a powerful new tool for matrix analysis in biological settings, where the relationship of observed quantities to more meaningful variables is often nonlinear and unknown.

structure of neural correlation | neural coding | Betti curves | clique topology | topological data analysis

Neural activity and connectivity data are often presented in the form of a matrix whose entries, C_{ij} , indicate the strength of correlation or connectivity between pairs of neurons, cell types, or imaging voxels. Detecting structure in such a matrix is a critical step toward understanding the organization and function of the underlying neural circuits. In this work, we focus on neural activity, whose structure may reflect the coding properties of neurons, rather than their physical locations within the brain. For example, place cells in rodent hippocampus act as position sensors, exhibiting a high firing rate when the animal's position lies inside the neuron's "place field," its preferred region of the spatial environment (1). Without knowledge of the coding properties, however, it is unclear whether such a geometric organization could be detected purely from the pattern of neural correlations. Alternatively, a correlation or connectivity matrix could be truly unstructured, such as the connectivity pattern observed in the fly olfactory system (2), indicating random network organization.

Can we distinguish these possibilities, using only the intrinsic features of the matrix C_{ij} ? The most common approach is to use standard tools from matrix analysis that rely on quantities, such as eigenvalues, that are invariant under linear change of basis. This strategy is natural in physics, where meaningful quantities should be preserved by linear coordinate transformations. In contrast, measurements in biological settings are often obtained as nonlinear transformations of the underlying "real" variables, whereas the choice of basis is meaningful and fixed. For example, basis elements might represent particular neurons or genes, and measurements (matrix elements) could consist of pairwise correlations in neural activity, or the coexpression of pairs of genes. Instead of change of basis, the relevant structure in these data

should be invariant under matrix transformations of the following form:

$$C_{ij} = f(A_{ij}), \quad [1]$$

where f is a nonlinear monotonic function (Fig. 1A). In the case of hippocampal place cells, f captures the manner in which pairwise correlations C_{ij} decrease with distance between place field centers (3). In less studied contexts, the represented stimuli—and the function f —may be completely unknown.

Unfortunately, eigenvalues are not invariant under transformations of the form (Eq. 1) (Fig. 1B and *SI Appendix*, Fig. S1). Although large random matrices have a reliable eigenvalue spectrum [e.g., Wigner's semicircle law (4)], it is possible that a random matrix with independent and identically distributed (i.i.d.) entries could be mistaken as structured, purely as an artifact of a monotonic nonlinearity (Fig. 1B).^{*} The results of eigenvalue-based analyses can thus be difficult to interpret, and potentially misleading.

Here, we introduce a new tool to reliably detect signatures of structure and randomness that are invariant under nonlinear monotone transformations of the form (Eq. 1). Using pairwise correlations of hippocampal place cells recorded during both spatial and nonspatial behaviors, we demonstrate that our method is capable of detecting geometric structure from neural activity alone. To our knowledge, this is the first example of a method

Significance

Detecting structure in neural activity is critical for understanding the function of neural circuits. The coding properties of neurons are typically investigated by correlating their responses to external stimuli. It is not clear, however, if the structure of neural activity can be inferred intrinsically, without a priori knowledge of the relevant stimuli. We introduce a novel method, called clique topology, that detects intrinsic structure in neural activity that is invariant under nonlinear monotone transformations. Using pairwise correlations of neurons in the hippocampus, we demonstrate that our method is capable of detecting geometric structure from neural activity alone, without appealing to external stimuli or receptive fields.

Author contributions: C.G., C.C., and V.I. designed research; C.G., E.P., C.C., and V.I. performed research; C.G., C.C., and V.I. analyzed data; and C.G., C.C., and V.I. wrote the paper.

The authors declare no conflict of interest.

This article is a PNAS Direct Submission.

Freely available online through the PNAS open access option.

¹C.C. and V.I. contributed equally to this work.

²To whom correspondence should be addressed. Email: vladimir.itskov@psu.edu.

This article contains supporting information online at www.pnas.org/lookup/suppl/doi:10.1073/pnas.1506407112/-DCSupplemental.

^{*}Note that the matrix $C = f(A)$ in Fig. 1B is also a random matrix, with i.i.d. entries drawn from the transformed distribution. Although the eigenvalue spectrum still converges to the Wigner semicircle distribution in the limit of large N (5), the rate of convergence depends on the nonlinearity f , allowing for large deviations from the semicircle distribution as compared with a normally distributed random matrix with the same N .

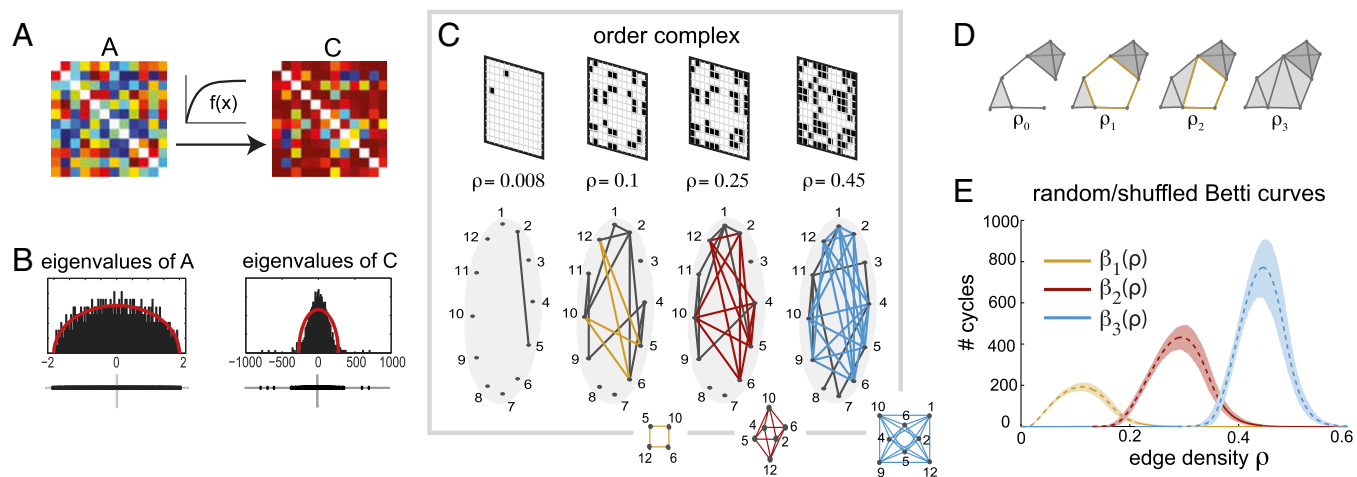


Fig. 1. Order-based analysis of symmetric matrices. (A) A symmetric matrix A is related to another matrix C via a nonlinear monotonically increasing function $f(x)$, applied entrywise. (B, Left) Distribution of eigenvalues for a random symmetric $N \times N$ matrix A , whose entries were drawn independently from the normal distribution with zero mean and variance $1/\sqrt{N}$ ($N=500$). (Right) Distribution of eigenvalues for the transformed matrix with entries $C_{ij} = f(A_{ij})$, for $f(x) = 1 - e^{-30x}$. Red curves show Wigner's semicircle distribution with matching mean and variance. (C, Top) The order complex of A is represented as a sequence of binary adjacency matrices, indexed by the density ρ of nonzero entries. (Bottom) Graphs corresponding to the adjacency matrices. Minimal examples of a 1-cycle (yellow square), a 2-cycle (red octahedron), and a 3-cycle (blue orthoplex) appear at $\rho=0.1, 0.25$, and 0.45 , respectively. (D) At edge density ρ_0 , there are no cycles. Cliques of size 3 and 4 are depicted with light and dark gray shading. As the edge density increases, a new 1-cycle is created, persists, and is eventually destroyed at densities ρ_1, ρ_2 , and ρ_3 , respectively. (E) For a distribution of 1,000 random $N \times N$ symmetric matrices ($N=88$), average Betti curves $\beta_1(\rho)$, $\beta_2(\rho)$, and $\beta_3(\rho)$ are shown (yellow, red, and blue dashed curves), together with 95% confidence intervals (shaded areas).

that detects geometric organization intrinsically from neural activity, without appealing to external stimuli or receptive fields.

Results

The only feature of a matrix that is preserved under the transformations (Eq. 1), for monotonically increasing f , is the relative ordering of its entries, as $C_{ij} < C_{kl}$ whenever $A_{ij} < A_{kl}$ (SI Appendix, Supplementary Text). We refer to this combinatorial information as the “order complex,” $\text{ord}(C)$. It is convenient to represent the order complex as a nested sequence of graphs, where each subsequent graph includes an additional edge (ij) corresponding to the next-largest matrix entry C_{ij} (Fig. 1C). Any quantity computed from the order complex is automatically invariant under the transformations (Eq. 1), because $\text{ord}(A) = \text{ord}(C)$. We found that the arrangement of “cliques” (all-to-all connected subgraphs) in the order complex of a matrix can be used in lieu of eigenvalues to detect random or geometric structure.

“Clique topology” provides a systematic measure of how cliques fit together and overlap across the entire order complex. The topological structure of cliques in a graph can be quantified by first “filling in” all cliques, and then counting noncontractible cycles, i.e., arrangements of cliques which bound “holes.” Minimal examples of 1-, 2-, and 3-cycles are shown in Fig. 1C (Inset). A 1-cycle bounds a 2D area, a 2-cycle bounds a 3D volume, and a 3-cycle bounds a 4D region (SI Appendix, Supplementary Text). As the edge density ρ increases, new cycles are created, modified, and eventually destroyed (Fig. 1D). One can track these changes by computing a set of Betti numbers (6, 7), β_m , which count the independent m -cycles in each graph after all cliques have been filled in. The Betti numbers across all graphs in an order complex yield “Betti curves,” $\beta_m(\rho)$ (Materials and Methods and SI Appendix, Supplementary Text).

Detection of Random Organization. Although the details of individual graphs in the order complex may be sensitive to noise in the matrix entries, we found that clique topology provides robust signatures that can be used to distinguish structure from randomness. In the case of a random symmetric matrix with i.i.d. entries, the corresponding order complex is a sequence of Erdős–Rényi random graphs. We found that the Betti curves $\beta_m(\rho)$ are remarkably

reliable for such matrices (Fig. 1E), and display a characteristic unimodal shape with peak values that increase with m ($m \ll N$). This reliability has been theoretically predicted (8, 9) and makes it possible to robustly distinguish random from nonrandom structure in the presence of a monotone nonlinearity (Eq. 1). Unsurprisingly, correlation matrices obtained from finite samples of N independent random variables display the same characteristic Betti curves as random symmetric $N \times N$ matrices (SI Appendix, Fig. S2). Note that computing low-dimensional ($m \leq 3$) Betti curves for matrices of size $N \sim 100$ is numerically tractable due to recent advances in computational topology (7, 10, 11).

Detection of Geometric Organization. If a correlation or connectivity matrix is not random, what kind of structure can one detect? Uncovering “geometric” structure is especially important in neuroscience, because it indicates that neurons encode geometrically organized stimuli. For example, orientation-tuned neurons (12) and hippocampal place cells (1) have correlations that decrease with distance between represented angles or locations in the environment, respectively. This is easy to see by correlating neural responses directly to the relevant stimuli. However, it is unclear whether it is even possible to detect such an organization from pairwise correlations among neurons alone—without a priori knowledge of the represented stimulus space. A further difficulty is to detect geometric organization that is invariant under nonlinear monotone transformations of the matrix entries.

To our surprise, we found that the ordering of matrix entries encodes geometric features, such as dimension (Fig. 24). For larger matrices, the precise dimension may be difficult to discern in the presence of noise. Nevertheless, the organization of cliques in the order complex carries signatures of an underlying Euclidean geometry, irrespective of dimension. For example, the triangle inequality, $\|x - z\| \leq \|x - y\| + \|y - z\|$, implies that if two edges of a triangle are present in the order complex at some edge density ρ , there is a higher probability of the third edge also being present. Intuitively, this means that cliques in the order complex will be more prominent for geometric compared with random matrices, and cycles will be comparatively short-lived, as cliques cause holes to be more readily filled in (13).

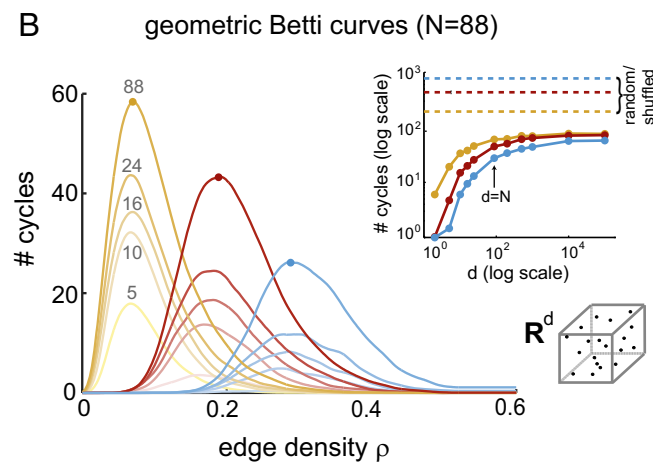
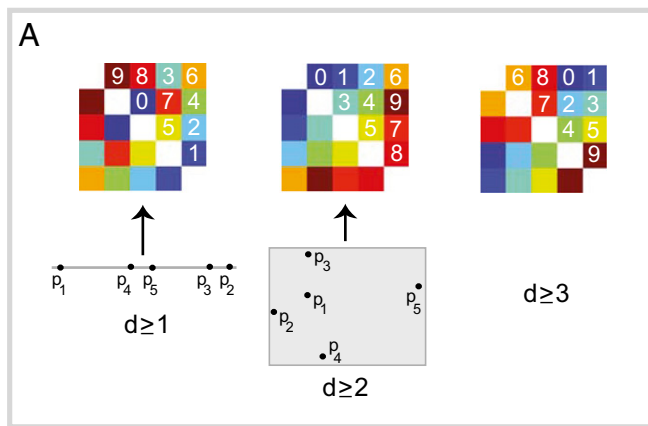


Fig. 2. Geometric structure is encoded in the ordering of matrix entries. (A) Three 5×5 symmetric matrices with distinct order complexes; the 10 off-diagonal matrix values in each are ordered from 0 to 9. An ordering of matrix values can be obtained from an arrangement of points, p_i , in d -dimensional Euclidean space if $A_{ij} < A_{ki}$ whenever $\|p_j - p_i\| < \|p_k - p_i\|$. (Left) A matrix ordering that arises from points on a line. (Middle) An ordering that arises from points in the plane, but cannot be obtained from points on a line. (Right) An ordering that cannot arise from distances between points in one or two dimensions. (B) Betti curves for distributions of geometric matrices ($N=88$) in dimensions $d=5, 10, 16, 24$, and 88 . Mean Betti curves $\beta_1(\rho)$, $\beta_2(\rho)$, and $\beta_3(\rho)$ are shown (yellow, red, and blue curves), with darker (and higher) curves corresponding to larger d . Dots indicate peak values of $d=N$ curves. (Inset) Peak values of Betti curves for $N=88$ geometric matrices as a function of dimension. Beyond $d=N$, peak values increase very slowly and remain small compared with random/shuffled matrices with matching N (dashed lines). The last point on each curve corresponds to $d=100,000$.

To see whether clique topology can provide reliable signatures of geometric organization, we computed Betti curves for distributions of geometric matrices ($N=88$), generated from random points uniformly sampled from unit cubes of dimensions $d=5, 10, 16, 24$, and 88 , and having entries that decrease with distance (*Materials and Methods*). We then computed average Betti curves $\beta_1(\rho)$, $\beta_2(\rho)$, and $\beta_3(\rho)$ for each d , and found that they are stratified by dimension but retain characteristic features that are independent of dimension. In particular, the peak values of geometric Betti curves are considerably smaller than those of random symmetric matrices with matching parameters ($p < 0.001$), and decrease with increasing m (Fig. 2B). This pattern remains over the full range of tested dimensions (Fig. 2B, Inset). We conclude that Betti curves can, in principle, be used to distinguish geometric from random structure.

Signatures of Intrinsic Geometric Structure in Neural Activity. Can clique topology be used to detect geometric organization from pairwise correlations in noisy neural data? To answer this question, we examined correlations of hippocampal place cells in rodents during spatial navigation in a 2D open field environment. In this context, geometric structure is expected due to the existence of spatially localized receptive fields [place fields (1)] but has not previously been detected intrinsically using only the pattern of correlations.

We computed correlations from spike trains of simultaneously recorded neurons in area CA1 of dorsal hippocampus (*Materials and Methods*). Each pairwise correlation, C_{ij} , was obtained from the mean of a cross-correlogram on a timescale of $\tau_{\max} = 1$ s (*SI Appendix, Supplementary Methods*, and Fig. S3). The resulting matrix was then analyzed using clique topology (Fig. 3A). As expected, the Betti curves from place cell data were in close agreement to those of geometric matrices (Fig. 3B, Top), up to a small rightward shift that is likely due to noise (*SI Appendix, Fig. S4A*).

Although we found that qualitative geometric structure is robustly detectable, the precise dimension is sensitive to noise and currently difficult to estimate, even for low dimensions. For example, a geometric matrix in dimension $d=2$ exhibits higher-dimensional nonzero Betti curves if a fraction of the neurons have nongeometric correlations with the rest (*SI Appendix, Fig. S4B*). A post hoc analysis of the recorded place cells showed that 5–10% exhibited nonconvex place fields; this alone could account for the higher dimensions we observed. On the other hand, Betti curves of $d=2$ geometric matrices with up to 10% of the neurons having random correlations still lie in the $d \leq N$ geometric regime (*SI Appendix, Fig. S4B*).

We next compared the data Betti curves to shuffled controls, obtained by randomly permuting the matrix entries (*SI Appendix, Fig. S5 A and B*). Shuffling completely destroys any structure in the order complex, yielding distributions of Betti curves identical to those of random matrices (Fig. 1E). We found that the Betti curves from place cell data were an order of magnitude smaller than the mean Betti curves of the shuffled matrices, and well outside the 95% confidence intervals (Fig. 3B, Bottom). To quantify the significance of nonrandom structure, we used integrated Betti values as follows:

$$\bar{\beta}_m = \int_0^1 \beta_m(\rho) d\rho,$$

and verified that they were significantly smaller than those obtained from 1,000 trials of the shuffled controls ($P < 0.001$), but well within the confidence intervals for geometric controls (Fig. 3C).

To test whether the observed geometric organization was consistent across animals and recording sessions, we repeated these analyses for eight additional datasets from three different animals during spatial navigation (*SI Appendix, Fig. S6*). All but one of the nine datasets were consistent with the corresponding geometric controls, suggesting that geometric structure of correlations is a robust phenomenon during spatial navigation. We also repeated the analyses for different choices of the correlation timescale, τ_{\max} , ranging from 10 ms to 2 s, and observed similar results (Fig. 3D). As a further test of geometric organization, we computed the distribution of “persistence lifetimes” from the order complex of the open field correlation matrix (*SI Appendix, Supplementary Text*). The lifetime measures how long a hole persists as it evolves from one graph to the next in the order complex (Fig. 1D). Again, the data exhibited topological signatures that were far from random, but consistent with geometric organization (*SI Appendix, Fig. S7*).

To ensure that the observed correlation structure could not be explained by the differences in interactions of individual neurons with the “mean field” activity of the network, we performed an additional random control that preserves row and column sums of pairwise correlation matrices. Specifically, we computed Betti curves for matrices drawn from a weighted maximum entropy

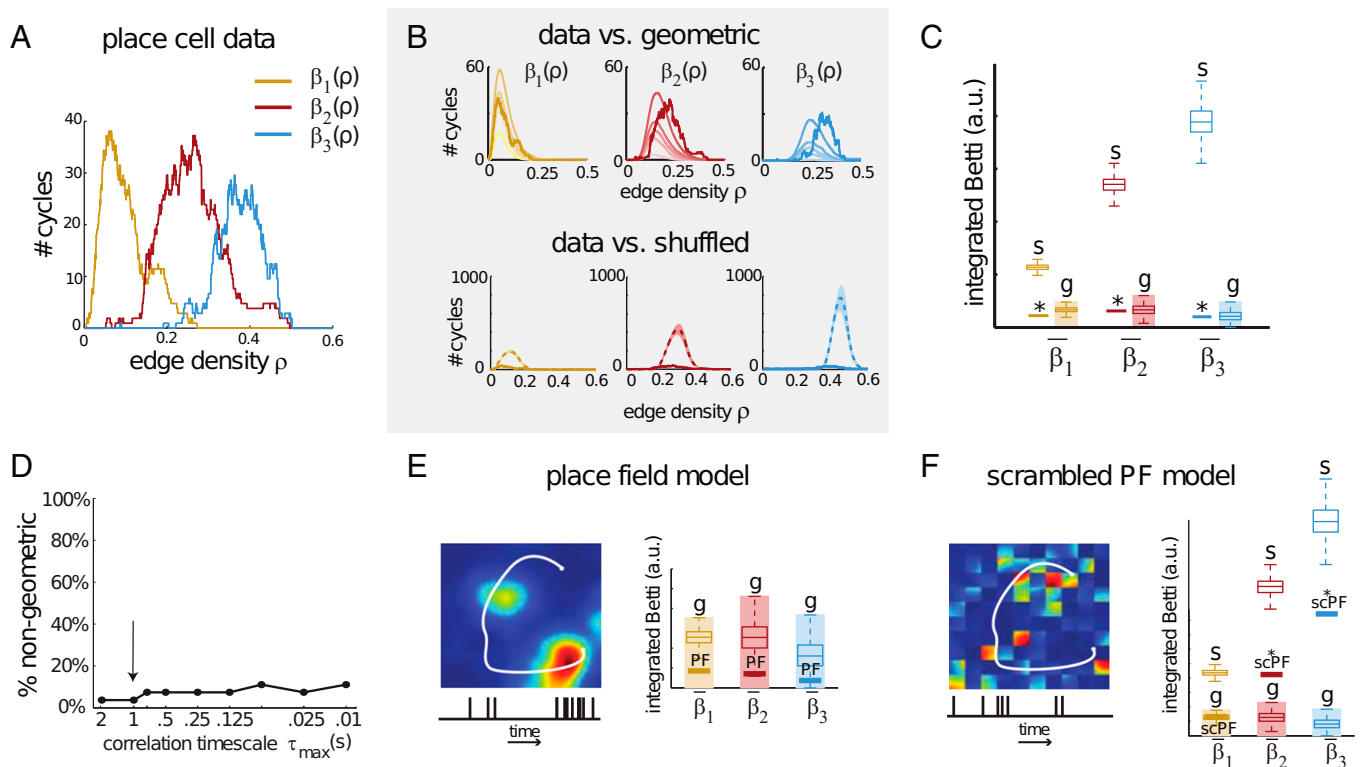


Fig. 3. Geometric structure of correlations for neurons with spatial receptive fields. (A) Betti curves of the pairwise correlation matrix for the activity of $N=88$ place cells in hippocampus during open-field spatial exploration. (B, Top) Betti curves from A (bold lines) overlaid on the mean geometric Betti curves from Fig. 2B. (Bottom) Comparison of Betti curves from A to those of shuffled correlation matrices (note the change in vertical scale). (C) Integrated Betti values $\bar{\beta}_m$ for the curves in A (solid lines), compared with standard box plots of integrated Betti values for the 1,000 shuffled [s] and geometric [g] controls displayed in B. The geometric box plots are shown for the highest dimension, $d=88$, whereas the shaded area indicates the confidence interval across all dimensions $d \leq 88$. Betti values for the place cell data are significantly nonrandom ($*P < 0.001$), and appear consistent with those of geometric matrices. (D) Percentage of nongeometric Betti values $\bar{\beta}_1, \bar{\beta}_2, \bar{\beta}_3$ for a range of correlation timescales τ_{\max} . Each point is an average over nine open-field recordings. The arrow indicates the timescale considered in A–C. (E, Left) A place field together with a cartoon trajectory (white) and simulated spike train (bottom). (Right) Integrated Betti values for correlations in the place field model (bold lines, labeled PF) lie within the geometric regime. (F, Left) A scrambled version of the place field in E. (Right) Integrated Betti values for the scrambled PF model (bold lines) are significantly nongeometric ($*P < 0.05$) for $\bar{\beta}_2$ and $\bar{\beta}_3$, whereas $\bar{\beta}_1$ is in the geometric regime. The Betti values are also significantly smaller than those of shuffled controls ($*P < 0.05$). Box plots for geometric and shuffled controls in E and F are the same as in C.

(WME) distribution, subject to the constraint that expected row sums match the original pairwise correlation matrix (SI Appendix, Fig. S5 C and D). The Betti curves and persistence lifetimes of the WME controls were similar to those of random symmetric matrices (SI Appendix, Fig. S8), showing that the nonrandom structure in the data does not arise from the fact that some neurons have higher levels of correlation with the population as a whole.

Scrambled Place Fields Yield Nongeometric Correlations. Are the spatial coding properties of place cells sufficient to account for the observed geometric organization of correlations during spatial navigation? Or, alternatively, does this structure reflect finer features of the correlations, beyond what is expected from place fields alone? To address this question, we computed place fields $F_i(\mathbf{x})$ for each place cell from the same data used in Fig. 3A, together with the animal's 2D spatial trajectory $\mathbf{x}(t)$ (SI Appendix, Supplementary Methods). We then generated synthetic spike trains for each neuron as inhomogeneous Poisson processes, with rate functions $r_i(t)$ given by the simple place field model as follows:

$$r_i(t) = F_i(\mathbf{x}(t)), \quad [2]$$

where $\mathbf{x}(t)$ is the animal's actual trajectory (Fig. 3E). By design, the synthetic spike trains preserved the influence of place fields, but discarded all other features of the data, including precise spike timing and any nonspatial correlates. Perhaps unsurprisingly, Betti

curves derived from the place field model reproduced all of the signatures of geometric organization (Fig. 3E and SI Appendix, Fig. S9 B and C), indicating that place fields alone could account for the results observed in the open field data.

We next asked whether the geometry of place fields was necessary, or whether the Betti curves during spatial navigation could be attributed to an even more basic feature of the data, which is that each neuron is driven by the same global signal, $\mathbf{x}(t)$, filtered by a cell-specific function $F_i(\mathbf{x})$. To answer this question, we scrambled each place field by permuting the values of $F_i(\mathbf{x})$ inside “pixels” of a 100×100 grid, creating nongeometric receptive fields $\tilde{F}_i(\mathbf{x})$ (SI Appendix, Fig. S9D; a 10×10 scrambling is shown in Fig. 3F for clarity). We then generated spike trains from the actual trajectory, as in Eq. 2, but using the scrambled place fields $\tilde{F}_i(\mathbf{x})$. For this model, we found that the second and third Betti curves were far outside of the geometric regime, whereas the first Betti curve $\beta_1(\rho)$ was insufficient to rule out geometric organization (Fig. 3F and SI Appendix, Fig. S9 E–H). We obtained similar results after scrambling on a 10×10 grid (SI Appendix, Fig. S10). We conclude that the geometric signatures observed during spatial navigation reflect the geometry of place fields and are not simply a consequence of neurons being driven by the same global signal, $\mathbf{x}(t)$. Nevertheless, each of the Betti curves for the scrambled place field model was also significantly smaller than those of random controls (Fig. 3F; $P < 0.001$), suggesting that neurons controlled by a global

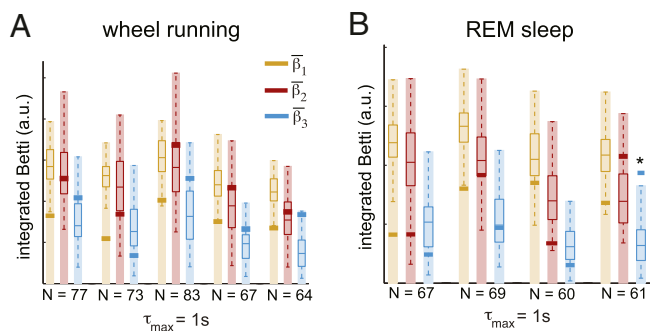


Fig. 4. Geometric organization in hippocampus during nonspatial behaviors. (A) Integrated Betti values $\bar{\beta}_1$, $\bar{\beta}_2$, and $\bar{\beta}_3$ (bold yellow, red, and blue lines) for five recordings from two animals, during wheel running. N indicates the number of neurons in each recording. Box plots indicate the distributions of Betti values for 100 geometric controls with matching N and dimension $d=N$. Shaded regions indicate confidence intervals for the full geometric regime, with $d \leq N$. (B) Integrated Betti values for four recordings from two animals, during REM sleep. One Betti value was significantly nongeometric ($*P < 0.05$).

signal via nongeometric receptive fields do exhibit nonrandom structure in their pairwise correlations.

Evidence of Geometric Organization During Nonspatial Behaviors.

The above results suggest that geometric structure in place cell correlations is a consequence of position coding and is not necessarily expected during nonspatial behaviors. To see whether this is true, we repeated our analyses on neural activity recorded during two nonspatial conditions: wheel running and rapid eye movement (REM) sleep. Surprisingly, we found that the Betti curves were again highly nonrandom (SI Appendix, Fig. S11), and consistent with geometric organization across all five wheel running recordings and three out of four sleep recordings (Fig. 4). These findings suggest that geometric organization on a timescale of $\tau_{\max} \sim 1$ s is a property of the underlying hippocampal network, and not merely a byproduct of spatially structured inputs. At much finer timescales, however, geometric features appear to deteriorate in both REM sleep and wheel-running conditions (SI Appendix, Fig. S12), in contrast to the open-field data (SI Appendix, Fig. S13).

Discussion

We have developed a novel tool for detecting structural features of symmetric matrices that are invariant under the transformations most commonly observed in neural systems. We have shown that this method can reliably detect both geometric and random structure in the presence of an unknown nonlinearity. Our approach exploits the little-known fact that the ordering of matrix entries, irrespective of their actual values, carries significant information about the underlying matrix organization. Unlike eigenvalues, which can be badly distorted by monotone nonlinearities, the information encoded in the order complex is invariant.

Applying techniques from computational topology, relevant features can be extracted from the order complex that enable robust detection of geometric (or random) structure. In contrast to previous instances of topological data analysis (14–20), our method relies on the statistical properties of cycles, as captured by Betti curves and persistence lifetime distributions, and is used as a generic tool for matrix analysis, rather than the analysis of point cloud data. Although the precise dimension associated to geometric data is currently difficult to estimate, this situation should improve once we gain a better understanding of how Betti curves and persistent cycles are distorted by different types of noise.

In this work, we have emphasized two extremes: geometric vs. random. In many cases, however, correlations may be structured in a nonrandom, but also nongeometric, manner. One example of this

is the scrambled place field model. Here, the existence of a global signal controlling the firing of all neurons introduced nonrandom relationships among the entries of the pairwise correlation matrix, and the Betti curves were able to distinguish this case from both the geometric and random controls. It is likely that many kinds of structure leave their fingerprints on the ordering of matrix elements and can thus in principle be detected with our methods.

In summary, we found that geometric organization of hippocampal place cell activity—a prerequisite for the existence of spatial receptive fields—can be detected from pairwise correlations alone, without any a priori knowledge about the nature of receptive fields. Using simulated data from a model, we confirmed that such geometric structure would be observed as a result of realistic place fields, but would not arise from nongeometric (“scrambled”) place fields. Perhaps surprisingly, we also found geometric organization in correlations during wheel running and REM sleep. We suggest that clique topology is a powerful new tool for matrix analysis, and one that is especially useful in biological settings, to detect relevant structure in the presence of unknown nonlinearities.

Materials and Methods

Experimental Data. All procedures were approved by the Janelia Research Campus Institutional Animal Care and Use Committee. Spike trains of neurons in area CA1 of rodent hippocampus were recorded during three behavioral conditions: (i) spatial navigation in a familiar, 2D, 1.5 m \times 1.5-m square box environment; (ii) wheel running in the context of a delayed alternation task, as described in refs. 21 and 22; and (iii) REM sleep. Experimental procedures have been previously described in refs. 21 and 23. SI Appendix, Supplementary Methods, contains further details related to the data, the computation of pairwise correlations, and the place field (PF) and scrambled PF models.

Clique Topology. We performed topological data analysis on pairwise correlation matrices (SI Appendix, Supplementary Methods) as well as random and geometric “control” matrices (below). Here, we describe the general procedure; for more detailed explanations, see SI Appendix, Supplementary Text.

Random and Geometric Matrices. For each symmetric matrix C we considered three types of controls: shuffled (or “random”) control matrices, WME control matrices, and geometric matrices. “Shuffled matrices” were created by randomly permuting the $\binom{N}{2}$ off-diagonal elements of C . Because only the ordering of matrix elements is considered in the subsequent topological analyses, this is equivalent to considering random symmetric matrices with i.i.d. entries, whose corresponding order complex is a sequence of nested Erdős–Rényi random graphs. “WME matrices” were obtained by sampling the maximum entropy distribution on weighted graphs with constrained mean degree sequence induced by C . This distribution was previously described in ref. 24 (SI Appendix, Fig. S5).

“Geometric matrices” were obtained by sampling a set of N i.i.d. points uniformly distributed in the d -dimensional unit cube $[0,1]^d \subset \mathbb{R}^d$, for $d \leq N$. The matrix entries were then given by $C_{ij} = -\|\rho_i - \rho_j\|$, where the minus sign ensures that they monotonically decrease with distance, as expected for geometrically organized correlations.

Order Complex. For any $N \times N$ symmetric matrix A with distinct entries, the order complex $\text{ord}(A)$ is a sequence of graphs:

$$G_0 \subset G_1 \subset \dots \subset G_{\binom{N}{2}},$$

where G_0 is the graph having N vertices and no edges, G_1 has a single edge (ij) corresponding to the highest off-diagonal matrix value A_{ij} , and each subsequent graph has an additional edge for the next-highest off-diagonal matrix entry. The graphs $\{G_k\}$ can also be indexed by the edge density, $\rho = k / \binom{N}{2} \in [0,1]$, where k is the number of edges in the graph G_k .

Betti Curves. A clique in a graph is an all-to-all connected set of vertices. For each graph G in the order complex $\text{ord}(A)$, we compute simplicial homology groups $H_m(X(G), \mathbb{Z}_2)$ for $m=1,2$, and 3, where $X(G)$ is the clique complex of G . We call this the clique topology of G , to distinguish it from the usual graph topology. The dimensions of the homology groups $H_m(X(G), \mathbb{Z}_2)$, yield the Betti

numbers β_m . Indexing the graphs by edge density ρ , we organize the Betti numbers across all graphs in the order complex into Betti curves $\beta_1(\rho)$, $\beta_2(\rho)$, and $\beta_3(\rho)$.[†] The Betti curves provide a summary of the topological features of the matrix A .

Computations. All software for computing clique topology is freely available in our Matlab package CliqueTop (26). To compute Betti curves for a matrix A , we begin by finding all maximal cliques of up to five vertices (those are needed to compute β_3) for each graph G_ρ , with $\rho \leq 0.6$. The resulting lists are then input into Perseus, a computational topology software package implemented by Vidit Nanda (27); this software builds on work by Mischaikow and Nanda (28) using discrete Morse theory to reduce the sizes of simplicial complexes before performing persistent homology computations.

Integrated Betti Values. To facilitate the comparison of Betti curves to control matrices, we integrate the Betti curves with respect to graph density: $\bar{\beta}_m = \int_0^1 \beta_m(\rho) d\rho$. The values $\bar{\beta}_1$, $\bar{\beta}_2$, and $\bar{\beta}_3$ were computed for each dataset. For distributions of shuffled and geometric control Betti curves, the resulting integrated Betti values are summarized in box-and-whisker plots. We used standard box plots in Matlab, with bottom, middle, and top horizontal lines on the boxes denoting first quartile (Q_1 , 25th percentile), median (50th percentile), and third quartile (Q_3 , 75th percentile) boundaries in the distributions of integrated Betti values; whereas the bottom and top whiskers denote $Q_1 - 1.5(Q_3 - Q_1)$ and $Q_3 + 1.5(Q_3 - Q_1)$, respectively.

[†]The Betti curve $\beta_0(\rho)$, which we have not used here, counts the number of connected components in each clique complex and may thus be useful for clustering (25).

Significance Threshold. Our threshold for rejecting the geometric hypothesis for a given integrated Betti value was obtained from the box-and-whisker plot for a distribution of 100 geometric matrices with matching N and dimension $d=N$. Specifically, we used the top whisker value, $Q_3 + 1.5(Q_3 - Q_1)$, as the significance threshold. The bottom whisker was not used, as Betti values lower than this are consistent with geometric matrices with smaller dimension d . In a normal distribution, 99.3% of the data lie within the whiskers, so that less than 0.4% of data points lie above the top whisker. Our integrated Betti values $\bar{\beta}_m$ for geometric controls, however, are not normally distributed. In the case of $\bar{\beta}_1$ and $\bar{\beta}_2$, the top whisker corresponds, on average, to the 98th percentile of the distribution. In the case of $\bar{\beta}_3$, the top whisker is just under the 97th percentile value. A data point above the top whisker is thus inconsistent with geometric controls with $P < 0.05$. For comparisons against shuffled/random control distributions, we computed the P value directly from the distribution, as in these cases we built the distributions from 1,000 trials, rather than just 100. Note that clique topology computations are much faster for matrices with random structure than for geometric matrices, because of differences in the statistics of the cliques.

ACKNOWLEDGMENTS. The authors would like to thank Dima Burago and Anton Petrunin for suggesting a simple proof for the $d \geq 3$ example in Fig. 2A. We thank the Holland Computing Center (University of Nebraska–Lincoln) and the Institute for Mathematics and its Applications (University of Minnesota) for providing resources that supported this work. This work was supported by National Science Foundation Grants DMS 1122519 (to V.I.) and DMS 1225666/1537228 (to C.C.), a Sloan Research Fellowship (to C.C.), Defense Advanced Research Projects Agency Young Faculty Award W911NF-15-1-0084 (to V.I.), and the Howard Hughes Medical Institute (E.P.).

- O'Keefe J, Dostrovsky J (1971) The hippocampus as a spatial map. Preliminary evidence from unit activity in the freely-moving rat. *Brain Res* 34(1):171–175.
- Caron SJ, Ruta V, Abbott LF, Axel R (2013) Random convergence of olfactory inputs in the *Drosophila* mushroom body. *Nature* 497(7447):113–117.
- Hampson RE, Byrd DR, Konstantopoulos JK, Bunn T, Deadwyler SA (1996) Hippocampal place fields: Relationship between degree of field overlap and cross-correlations within ensembles of hippocampal neurons. *Hippocampus* 6(3):281–293.
- Wigner EP (1958) On the distribution of the roots of certain symmetric matrices. *Ann Math* 67(2):325–327.
- Pastur L, Shcherbina M (2011) *Eigenvalue Distribution of Large Random Matrices*, Mathematical Surveys and Monographs (American Mathematical Society, Providence, RI), Vol 171.
- Hatcher A (2002) *Algebraic Topology* (Cambridge Univ Press, Cambridge, UK).
- Edelsbrunner H, Harer J (2008) *Surveys on Discrete and Computational Geometry*, Contemporary Mathematics (American Mathematical Society, Providence, RI), Vol 453, pp 257–282.
- Kahle M (2009) Topology of random clique complexes. *Discrete Math* 309(6):1658–1671.
- Kahle M, Meckes E (2013) Limit theorems for Betti numbers of random simplicial complexes. *Homology Homotopy Appl* 15(1):343–374.
- Zomorodian A, Carlsson G (2005) Computing persistent homology. *Discrete Comput Geom* 33(2):249–274.
- Harker S, Mischaikow K, Mrozek M, Nanda V (2014) Discrete Morse theoretic algorithms for computing homology of complexes and maps. *Found Comput Math* 14:151–184.
- Hubel DH, Wiesel TN (1959) Receptive fields of single neurones in the cat's striate cortex. *J Physiol* 148:574–591.
- Kahle M (2011) Random geometric complexes. *Discrete Comput Geom* 45(3):553–573.
- Curto C, Itskov V (2008) Cell groups reveal structure of stimulus space. *PLoS Comput Biol* 4(10):e1000205.
- Singh G, et al. (2008) Topological analysis of population activity in visual cortex. *J Vis* 8(8):1–18.
- Nicolau M, Levine AJ, Carlsson G (2011) Topology based data analysis identifies a subgroup of breast cancers with a unique mutational profile and excellent survival. *Proc Natl Acad Sci USA* 108(17):7265–7270.
- Dabaghian Y, Mémoli F, Frank L, Carlsson G (2012) A topological paradigm for hippocampal spatial map formation using persistent homology. *PLoS Comput Biol* 8(8):e1002581.
- Chan JM, Carlsson G, Rabadan R (2013) Topology of viral evolution. *Proc Natl Acad Sci USA* 110(46):18566–18571.
- Chen Z, Gomperts SN, Yamamoto J, Wilson MA (2014) Neural representation of spatial topology in the rodent hippocampus. *Neural Comput* 26(1):1–39.
- Petri G, et al. (2014) Homological scaffolds of brain functional networks. *J R Soc Interface* 11(101):20140873.
- Pastalkova E, Itskov V, Amarasingham A, Buzsáki G (2008) Internally generated cell assembly sequences in the rat hippocampus. *Science* 321(5894):1322–1327.
- Itskov V, Curto C, Pastalkova E, Buzsáki G (2011) Cell assembly sequences arising from spike threshold adaptation keep track of time in the hippocampus. *J Neurosci* 31(8):2828–2834.
- Wang Y, Romani S, Lustig B, Leonardo A, Pastalkova E (2015) Theta sequences are essential for internally generated hippocampal firing fields. *Nat Neurosci* 18(2):282–288.
- Hillar C, Wibisono A (2013) Maximum entropy distributions on graphs. arXiv:1301.3321 [math.ST].
- Chazal F, Guibas LJ, Oudot SY, Skraba P (2013) Persistence-based clustering in Riemannian manifolds. *J ACM* 60:41:1–41:38.
- Giusti C (2014) CliqueTop: Matlab package for clique topology of symmetric matrices. Available at github.com/nebneuron/clique-top. Accessed June 1, 2014.
- Nanda V (2013) The Perseus software project for rapid computation of persistent homology. Available at www.sas.upenn.edu/vnanda/perseus/index.html. Accessed June 1, 2014.
- Mischaikow K, Nanda V (2013) Morse theory for filtrations and efficient computation of persistent homology. *Discrete Comput Geom* 50:330–353.

SI Appendix

To accompany “Clique topology reveals intrinsic geometric structure in neural correlations.”

Chad Giusti, Eva Pastalkova, Carina Curto*, and Vladimir Itskov*

Contents:

1. Supplementary Methods (1 page)
2. Supplementary Figures 1-13 (13 pages)
3. Supplementary Text (19 pages)

Supplementary Methods

Here we present further details for the analyses involving hippocampal place cell data, along with descriptions of the place field and scrambled place field models.

Selection criteria for cells and recordings. During each of the three behavioral conditions (spatial navigation, wheel running, and REM sleep), only putative pyramidal cells whose average firing rates were in the 0.2-7 Hz range were used. Putative interneurons, defined as having an average firing rate above 7 Hz over an entire recording session, were excluded. Recordings with at least N=60 neurons satisfying these criteria were selected for the analyses. A total of 18 recordings from 5 animals met the selection criteria. These consisted of 9 “open field” spatial navigation data sets from three animals, 5 wheel running data sets from two animals, and 4 REM sleep data sets from two animals. Periods of REM sleep were detected from the local field potential using the ratio of total delta power (0.1-3 Hz) to total theta power (5-10 Hz) in the spectrogram of the EEG. Periods with delta/theta ratio less than 1 were considered REM sleep.

The number of cells and length of each recording were: N = 76 (16 min), N=81 (16 min), N=72 (63 min), N=88 (63 min), N=68 (59 min), N=64 (50 min), N=67 (50 min), N=74 (59 min), and N=66 (60 min) for spatial navigation; N=77 (26 runs, 6 min), N=73 (25 runs, 5 min), N=83 (13 runs, 5 min), N=67 (7 runs, 2 min), and N=64 (10 runs, 3 min) for wheel running; and N=67 (30 s), N=69 (4 min), N=60 (2.5 min), and N=61 (3.5 min) for REM sleep. The N=88 spatial navigation data set was used in Figure 3.

Computation of the pairwise correlation matrices. The cross-correlograms were computed as $c_{ij}(\tau) = \frac{1}{T} \int_0^T f_i(t) f_j(t+\tau) dt$, where $f_i(t)$ is the firing rate of the i -th neuron and T is the total duration of the considered time period. The normalized cross-correlation on a timescale of τ_{\max} was computed as

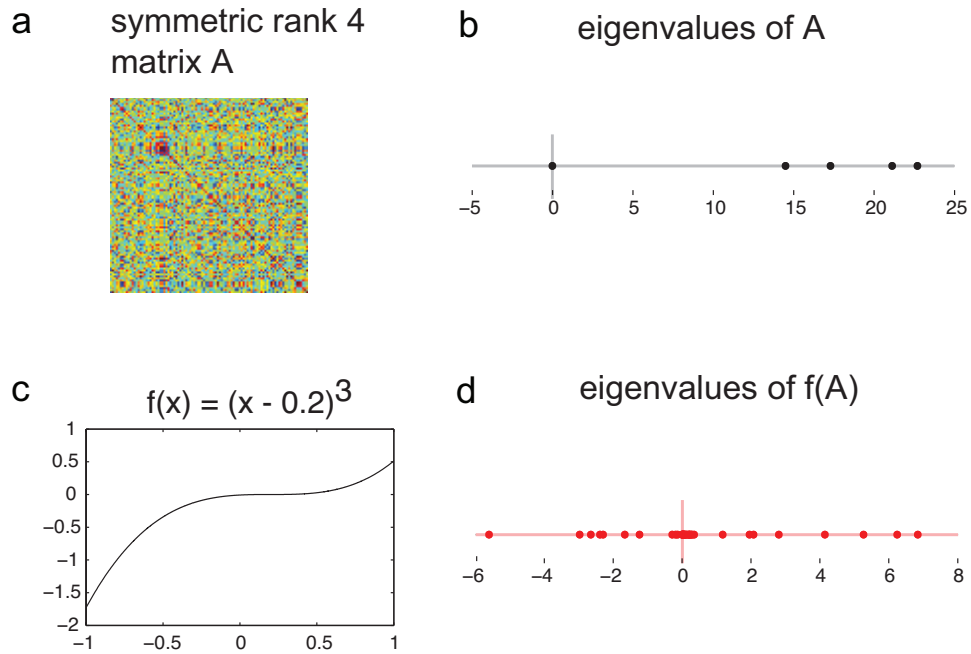
$$C_{ij} = \frac{1}{\tau_{\max} r_i r_j} \max \left(\int_0^{\tau_{\max}} c_{ij}(\tau) d\tau, \int_0^{\tau_{\max}} c_{ji}(\tau) d\tau \right),$$

where r_i is the average firing rate of the i -th neuron (see Supplementary Figure 3).

Simulated spike train data from PF and scrambled PF models. For each cell in the N=88 spatial navigation data set, place fields $F_i(\mathbf{x})$ were computed using a 100×100 grid of pixels. In each pixel, the number of spike events for each cell was normalized by the time spent at that location, and then smoothed with a 2-dimensional Gaussian ($\sigma = 5$ grid locations, see also Supplementary Figure 9). Simulated spike trains for the PF model were generated from the place fields as inhomogeneous Poisson processes with rate functions $r_i(t) = F_i(\mathbf{x}(t))$, using the animal’s original trajectory, $\mathbf{x}(t)$.

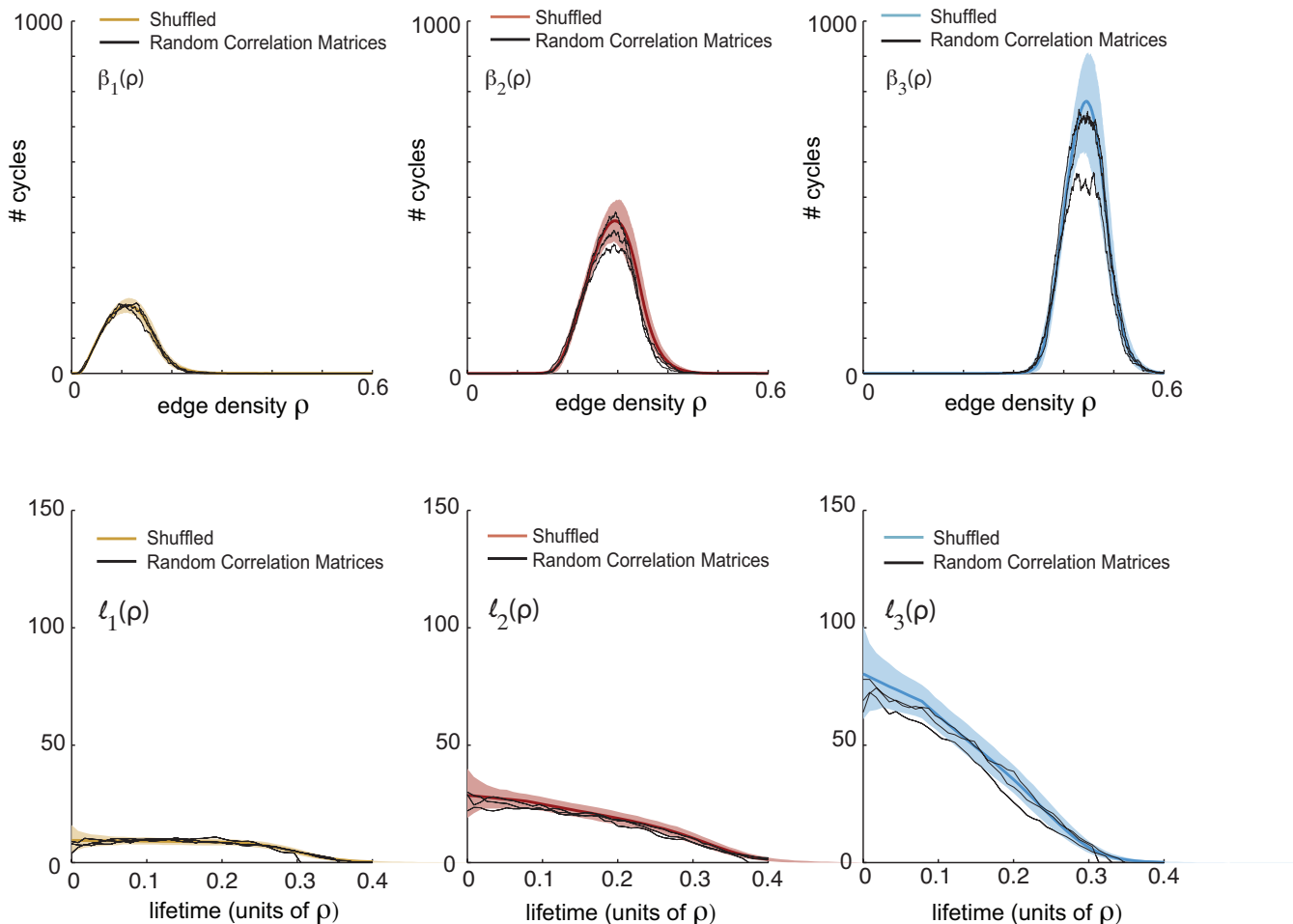
Scrambled place fields $\tilde{F}_i(\mathbf{x})$ were computed by randomly permuting the pixels in the 100×100 grid. A different permutation was used for each place field, in order to destroy the coherence of the spatial organization across the population. Similar spike trains for the scrambled PF model were again generated as inhomogeneous Poisson processes using the original trajectory, $\mathbf{x}(t)$, but with rate functions $r_i(t) = \tilde{F}_i(\mathbf{x}(t))$ given by the scrambled place fields (see Supplementary Figure 9). The simulated data sets were analyzed in Figure 3 at the correlation timescale $\tau_{\max} = 1\text{sec}$.

Supplementary Figures

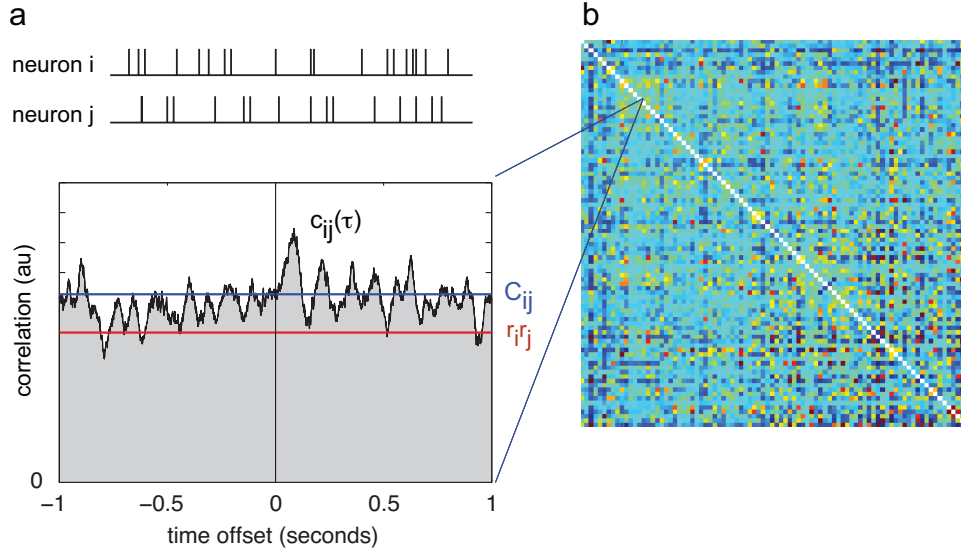


Supplementary Figure 1: Spectral signatures of matrix structure are destroyed by nonlinear monotonically increasing transformations. (a) A 100×100 symmetric matrix A with $\text{rank}(A) = 4$. (b) The spectrum of A includes four nonzero eigenvalues that are all positive. This is the signature that A has rank 4 and is positive semidefinite. (c) The graph of the monotonically increasing function $f(x) = (x - 0.2)^3$. (d) The spectrum of the matrix $f(A)$ contains many nonzero eigenvalues. The spectral signature that A has low-rank structure has been destroyed by f .

random correlation matrices vs. shuffled



Supplementary Figure 2: Topological properties of random correlation matrices are similar to those of random i.i.d. matrices. The $N \times N$ correlation matrix $C_{ij} = \text{corr}(X_i, X_j)$ was computed using 10,000 samples of $N = 88$ independent uniformly distributed random variables X_i . Each panel compares the Betti curves (top) and the persistence lifetimes (bottom) of the random correlation matrices to those of the random (shuffled) matrices. Each of the three black lines correspond to one instance of such a correlation matrix. Colored lines and shaded regions correspond to the mean curves and 95% confidence intervals for the random (shuffled) matrices.



Supplementary Figure 3: Computation of pairwise correlation matrices from spike train data.

(a) For a pair of spike trains $\{t_\ell^i\}_{\ell=1\dots n_i}$ and $\{t_\ell^j\}_{\ell=1\dots n_j}$ for neurons i and j (top), the cross-correlogram $ccg_{ij}(\tau)$ is computed as

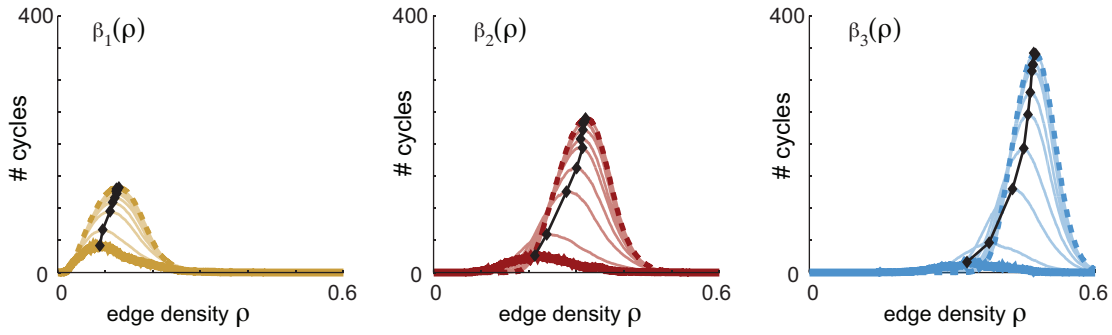
$$ccg_{ij}(\tau) = \frac{1}{T} \int_0^T f_i(t) f_j(t + \tau) dt,$$

where $f_i(t) = \sum_{\ell=1}^{n_i} \delta(t - t_\ell^i)$ is the instantaneous firing rate of the i -th neuron. The graph of a smoothed $ccg_{ij}(\tau)$ is displayed (black curve) along with the expected value of the cross-correlogram, $r_i r_j$ (red), for uncorrelated spike trains with matching firing rates, $r_i = n_i/T$. The pairwise correlations C_{ij} (blue line), with timescale τ_{\max} , were computed as

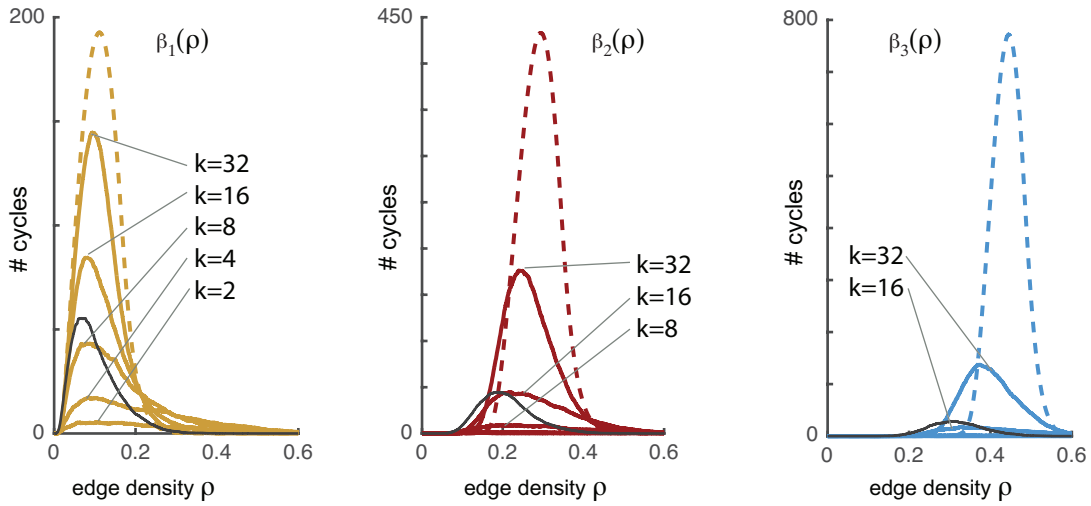
$$C_{ij} = \frac{1}{\tau_{\max} r_i r_j} \max \left(\int_0^{\tau_{\max}} ccg_{ij}(\tau) d\tau, \int_0^{\tau_{\max}} ccg_{ji}(\tau) d\tau \right)$$

The timescale $\tau_{\max} = 1$ sec was used in all but one panel of Figures 3 and 4, while a range of timescales from 10 ms to 2 sec appears in Figure 3d. (b) The 88×88 matrix C for the spatial exploration data used in Figure 3a,b,c. The entry $C_{14,15}$ corresponds to the cross-correlogram in panel (a).

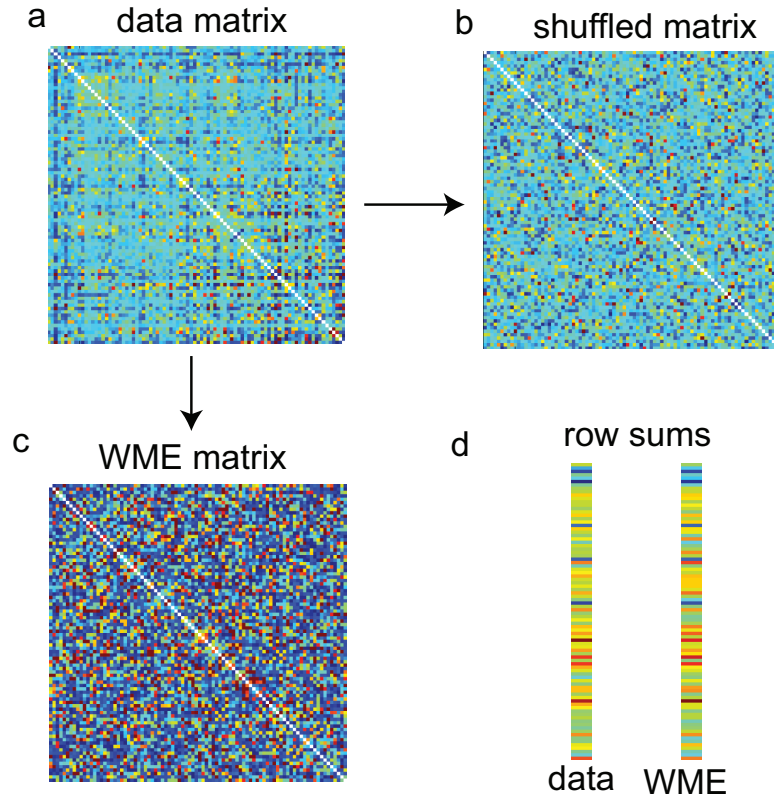
a Adding uncorrelated noise to the matrix



b Adding k “non-geometric” neurons



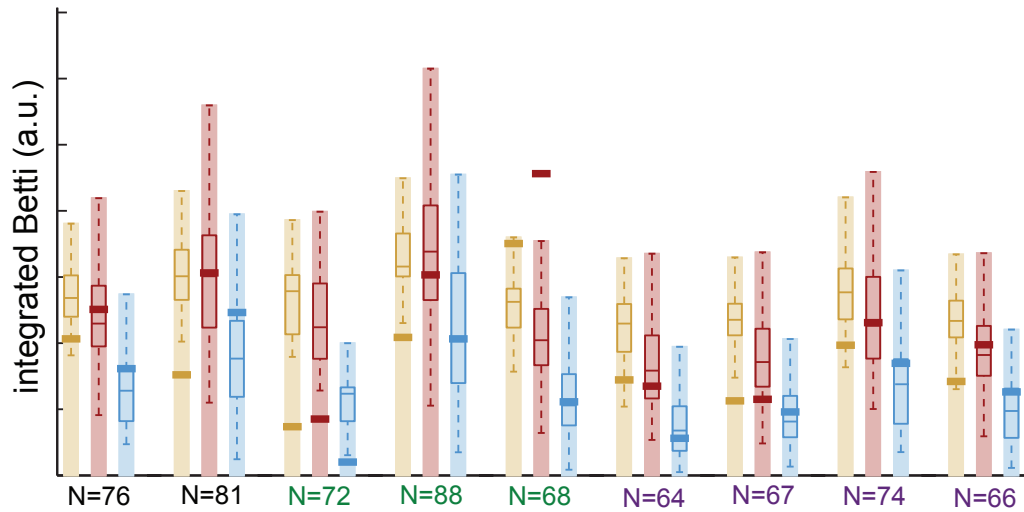
Supplementary Figure 4: The rightward and upward shift of the Betti curves can be explained by either adding noise to geometric matrices, or adding neurons that do not have any geometric organization to a geometrically organized population. (a) $N = 70$ random independent uniformly distributed points p_i in a d -dimensional unit cube were sampled in dimensions $d = N$. Noised geometric matrices were obtained as $A_{ij} = -\|p_i - p_j\| + (\nu\sqrt{d})g_{ij}$, where the terms g_{ij} were independent and normally distributed with zero mean and unit variance, and the noise strength ν took the following values: 0.01, 0.02, 0.03, 0.04, 0.05, 0.1, 0.25, 0.5. Each panel compares the Betti curves of the noised matrices (thin curves, stratified by the magnitude of the parameter ν) to those of the random matrices (dashed lines) and also the zero noise geometric matrices (thick curves). Black lines connect the maximum values of the mean curves for the different levels of noise. Small amounts of noise produce a rightward shift in the peak values of the Betti curves, while curves for $\nu = 0.5$ are indistinguishable from those of random matrices. (b) $N = 88$ random (uniformly distributed) points p_i were sampled in the 2-dimensional unit square. For each $k = 2, 4, 8, 16, 32$, the first k rows and columns of $A_{ij} = A_{ji} = -\|p_i - p_j\|$ were replaced with random values sampled independently from the uniform distribution on $[-\sqrt{2}, 0]$, thus yielding a matrix with k “non-geometric” neurons. Betti curves $\beta_1(\rho), \beta_2(\rho)$, and $\beta_3(\rho)$ (colored solid lines, stratified by k) represent averages over 35 trials. These Betti curves are shown superimposed over those of geometric matrices ($d = N$; solid black lines) and random matrices (dashed colored lines) of matching size. More than 10% of neurons must be non-geometric in order of the Betti curves to leave the geometric regime, but small numbers of non-geometric neurons increase the apparent dimension of the underlying space.



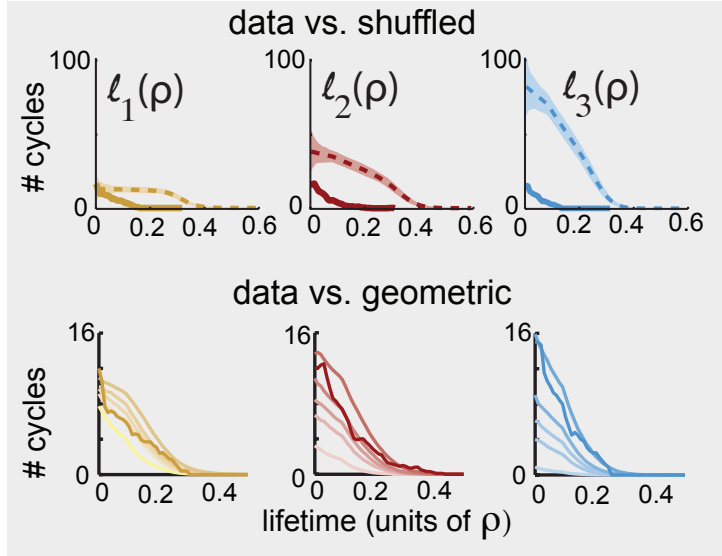
Supplementary Figure 5: Two types of random controls. (a) The matrix C_{ij} used in Figure 3a. (b) A shuffled matrix obtained by randomly permuting the $\binom{88}{2}$ off-diagonal elements of the symmetric matrix in panel (a). (c) A sample from the maximum entropy (WME) distribution on 88×88 symmetric matrices with prescribed expected values of row sums matching those of the matrix in panel (a). The distribution on each element (i, j) in the matrix is exponential with mean $\frac{1}{\theta_i + \theta_j}$ (Hillar & Wibisono, 2013 <http://arxiv.org/abs/1301.3321>). The parameters θ_i were obtained by solving the system of equations

$$\sum_{j \neq i} \frac{1}{\theta_i + \theta_j} = \sum_{j \neq i} C_{ij}, \quad \text{for } i = 1, \dots, N,$$

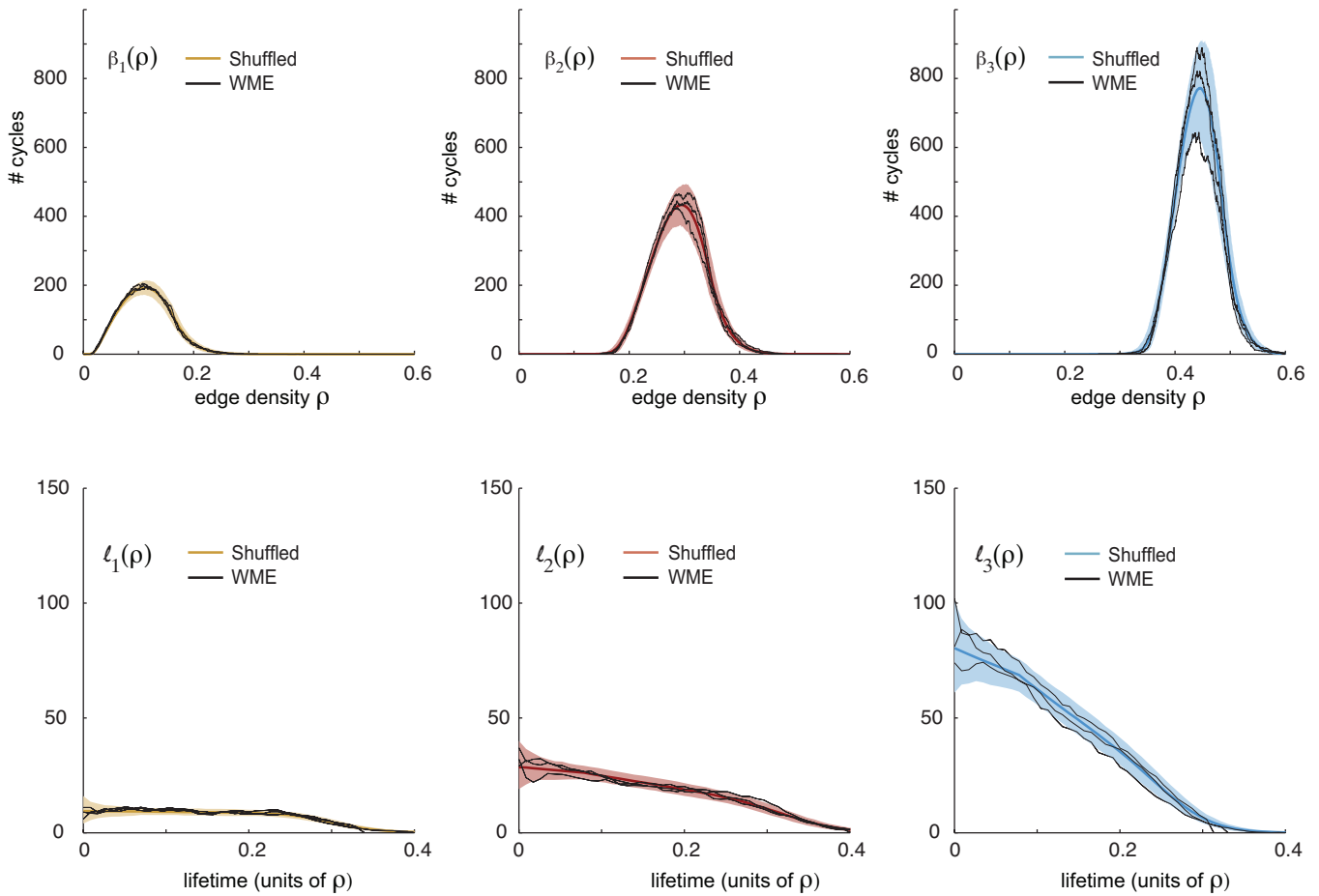
using standard gradient descent methods (Hillar & Wibisono, 2013). (d) (left) The row sums $\sum_{j \neq i} C_{ij}$ for the matrix in (a); (right) mean row sums for twenty samples from the distribution described in (c).



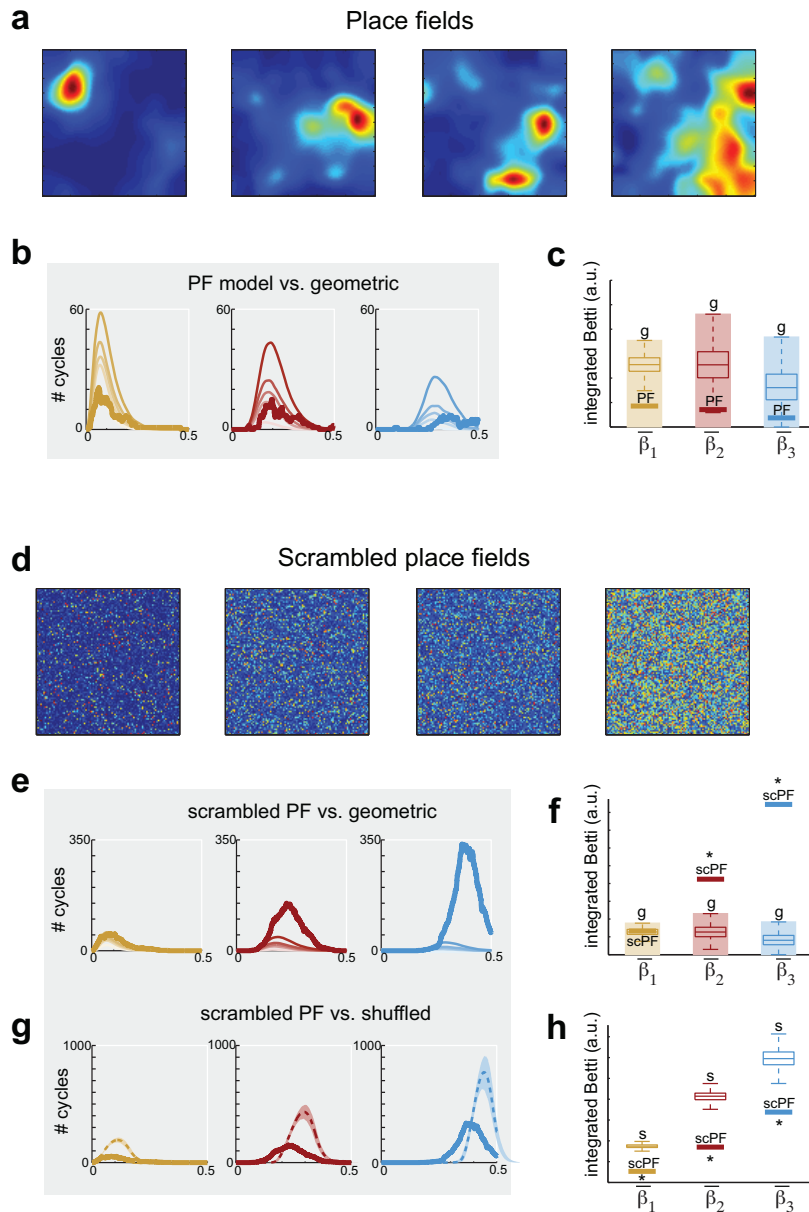
Supplementary Figure 6: Integrated Betti values obtained from neural activity during spatial navigation are consistent with those of geometric matrices. Integrated Betti values from place cell data are compared to geometric distributions with matching N across nine recordings of rat hippocampus during spatial navigation, obtained from three animals. The geometric box plots are shown for the dimension, $d = N$, while the shaded area indicates the confidence interval across the dimensions $d \leq N$. The number N of neurons is displayed in color (black, green, and purple) to indicate recordings from the same animal. Betti values for the place cell data are consistent with those of geometric matrices in all but one data set ($N = 68$).



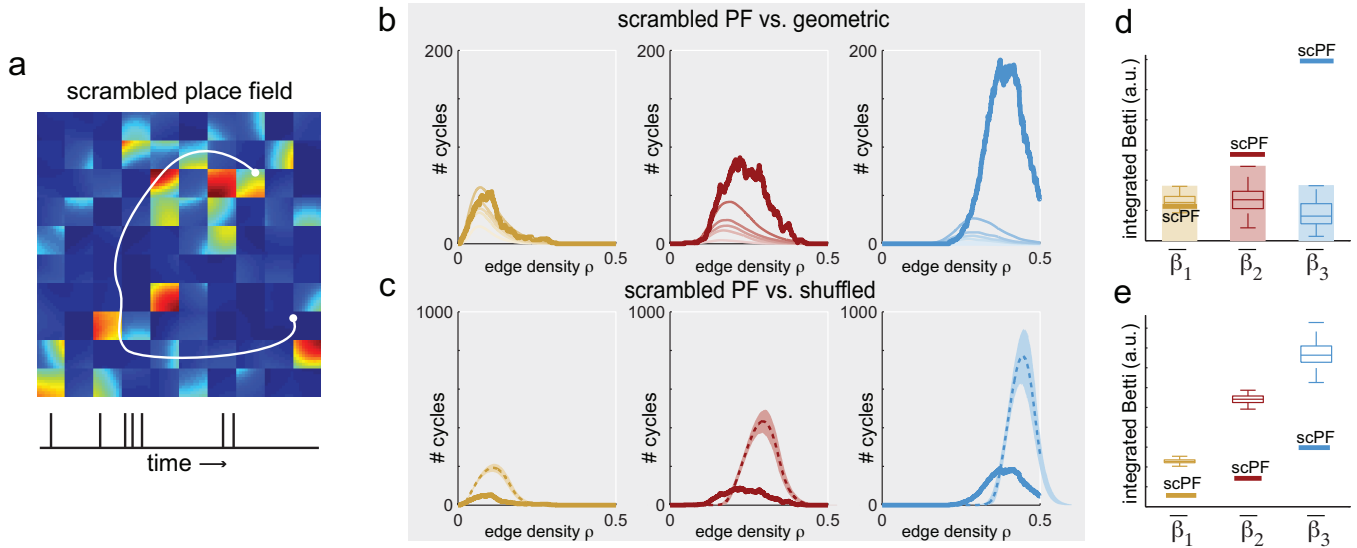
Supplementary Figure 7: The persistence lifetime distributions, computed from neural activity during spatial navigation resemble the geometric controls but are significantly below those of the shuffled matrices. Persistence lifetime distributions, $\ell_1(\rho)$ (yellow), $\ell_2(\rho)$ (red) and $\ell_3(\rho)$ (blue), computed from the same data set and controls as those used in Figure 3b. (Top) The lifetime distributions for the data (solid lines) fall off quickly, while those of the shuffled matrices are much broader (dashed lines are means over 1000 trials; shading shows the 95% confidence intervals). (Bottom) Here the data lifetime distributions (solid lines) are overlaid with the mean distributions (faint lines) for 1000 geometric matrices in each dimension $d = 5, 10, 16, 24,$ and 88 . As with the geometric Betti curves, the persistence lifetime distributions for geometric matrices are stratified by dimension, with the top curves corresponding to the highest dimension.



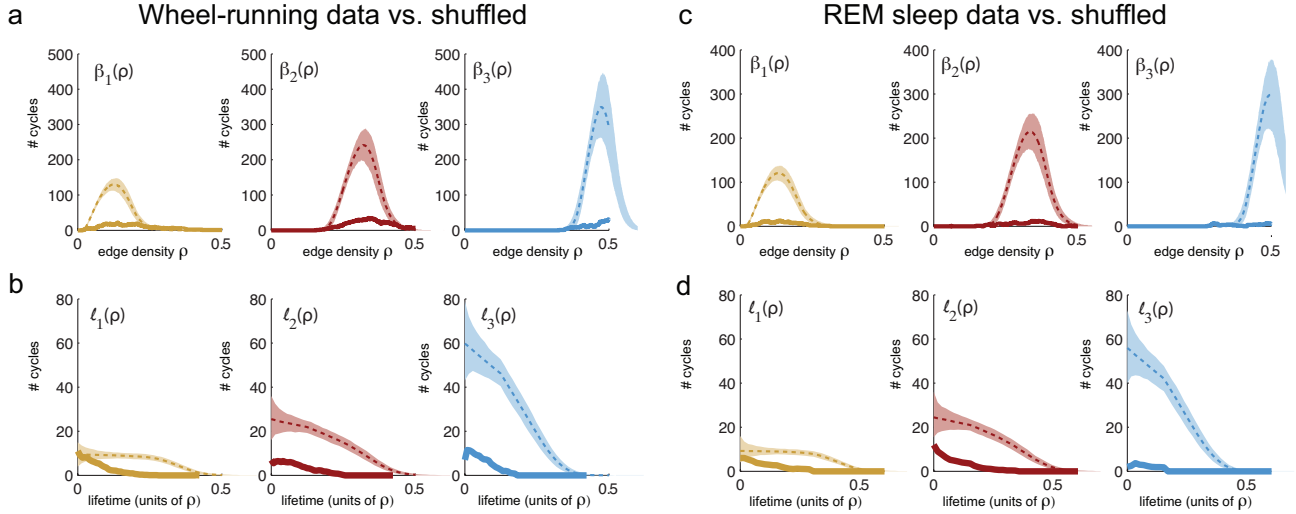
Supplementary Figure 8: Clique topology of WME matrices, sampled from the maximum entropy distribution with prescribed row sums, is similar to that of random (shuffled) matrices. Comparison of Betti curves (top) and persistence lifetimes (bottom) for WME matrices computed using the matrix C_{ij} used in Figure 3a. Each panel compares the Betti curves (top) and the persistence lifetimes (bottom) of the WME matrices, computed using the matrix C_{ij} used in Figure 3a, to those of the random (shuffled) obtained from the same C_{ij} . Each of the three black lines correspond to one sampling of a WME matrix. Colored lines and shaded regions correspond to the mean curves and 95% confidence interval for the shuffled matrices.



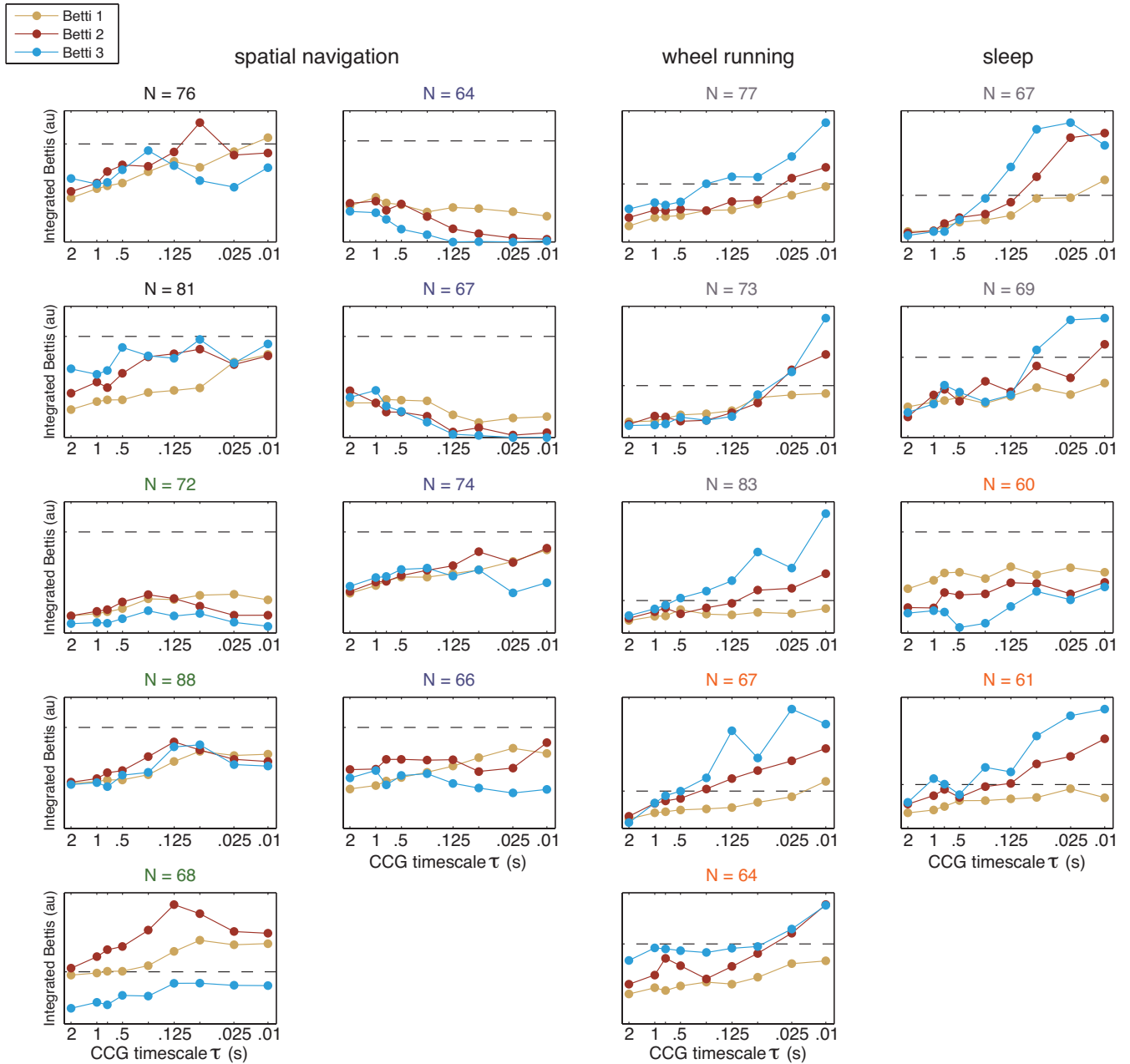
Supplementary Figure 9: (a) Example of several place fields computed from spike trains during spatial exploration in the $N=88$ data set. (b) Betti curves (bold lines) computed from the simulated spike trains ($\tau_{\max} = 1sec$) for the place field model versus the geometric Betti curves (thin lines stratified by dimensions). (c) Integrated Betti values (bold lines, labelled PF) for the curves in panel (b) lie in the geometric regime, in agreement with those of the original data. (d) The scrambled place fields corresponding to those in panel (a). These were obtained by sub-dividing the square into a 100×100 grid and randomly permuting each pixel. The permutations were independent for each cell. (e) Betti curves (bold lines) derived from the spike trains ($\tau_{\max} = 1sec$) generated using the scrambled PF model versus the geometric Betti curves (thin lines stratified by dimensions). (f) Integrated Betti values from the scrambled PF model (bold lines, labelled scPF) lie outside of the the significance threshold (see Supplementary Methods) for the geometric regime for $\bar{\beta}_2$ and $\bar{\beta}_3$. (g) Betti curves (bold lines) derived from the spike trains ($\tau_{\max} = 1sec$) generated using the Scrambled PF model are significantly smaller than those of shuffled controls. (h) Integrated Betti values derived from from the scrambled PF model (bold lines, labelled scPF) are outside the 99.9% confidence intervals for the shuffled matrices. Box plots for shuffled matrices are the same as in Figure 3c.



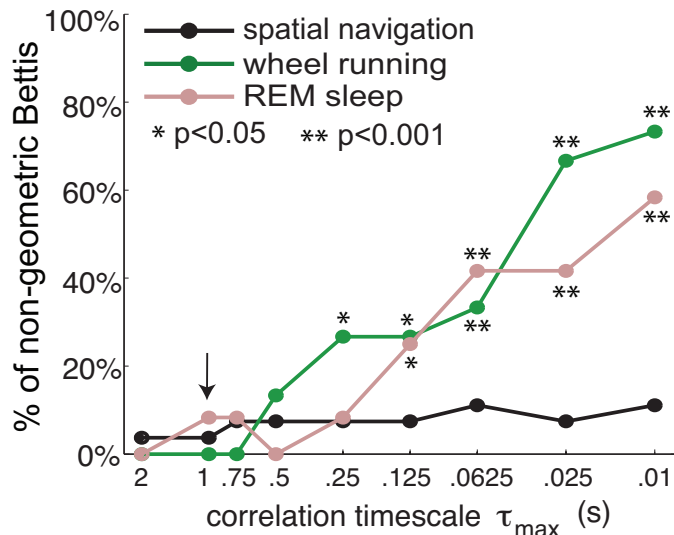
Supplementary Figure 10: Betti curves and summary stats for the 10x10 grid scrambled place fields. (a) A single scrambled place field corresponding to the place field in Figure 3e. The scrambling is performed on a 10×10 grid. A cartoon trajectory (white) is displayed together with the corresponding spike train (bottom). (b) Betti curves from the scrambled place field model (bold lines) lie outside the geometric regime for β_2 and β_3 . (c) Betti curves for the scrambled place field model are significantly smaller than the shuffled controls. (d) Integrated Betti values (bold lines, labelled scPF) for the scrambled place field model also lie outside of the significance threshold (see Supplementary Methods) for the geometric regime for $\bar{\beta}_2$ and $\bar{\beta}_3$, while $\bar{\beta}_1$ is in the geometric regime. (e) Integrated Betti values (bold lines, labelled scPF) for the scrambled place field model are outside the 99.9% confidence intervals for the shuffled matrices. Box plots for geometric and shuffled matrices are the same as in Figure 3c.



Supplementary Figure 11: The clique topology of spike train correlations during wheel running and REM sleep is significantly non-random as compared to shuffled matrices. (a) Comparison of the data Betti curves (solid lines) for the spike trains during wheel running ($N=73$ in Figure 4a) to those of shuffled correlation matrices (dashed lines are means over 1000 trials and shading shows 95% confidence intervals, as in Figure 1e). For each $m = 1, 2, 3$, the data Betti curves are orders of magnitude smaller than those of the shuffled curves. (b) Persistence lifetime distributions (solid lines) for the same data as in (a), $\ell_1(\rho)$ (yellow), $\ell_2(\rho)$ (red) and $\ell_3(\rho)$ (blue). The lifetime distributions for the data fall off quickly, while those of the shuffled matrices are much broader (dashed lines are means over 1000 trials; shading shows the 95% confidence intervals). (c) Comparison of the Betti curves (solid lines) for spike train correlations during REM sleep ($N=67$ in Figure 4b) to those of shuffled correlation matrices (dashed lines are means over 1000 trials and shading shows 95% confidence intervals, as in Figure 1e). For each $m = 1, 2, 3$, the data Betti curves are orders of magnitude smaller than those of the shuffled curves. (d) Persistence lifetime distributions (solid lines) for the same data as in (c). The lifetime distributions for the data fall off quickly, while those of the shuffled matrices are much broader (dashed lines are means over 1000 trials; shading shows the 95% confidence intervals).



Supplementary Figure 12: Integrated Betti values across a range of correlation timescales in spatial navigation, wheel running, and REM sleep data sets. For each of the datasets, and each $m = 1, 2, 3$, the integrated Betti number $\bar{\beta}_m = \int_0^1 \beta_m(\rho) d\rho$ was normalized by its significance threshold $b_m = Q_3 + 1.5 \times (Q_3 - Q_1)$ (see Supplementary Methods) that was obtained from the distribution of the integrated geometric Betti curves $\bar{\beta}_m^{\text{geom}} = \int_0^1 \beta_m^{\text{geom}}(\rho) d\rho$ in dimension $d = N$, where N was the number of cells. Each of the curves (yellow, red and blue) correspond to the values of $\bar{\beta}_m/b_m$ in dimensions $m = 1, 2, 3$ respectively. The dashed line marks the line $\bar{\beta}_m = b_m$; the appropriate integrated Betti numbers were deemed consistent with geometric distribution if they lay below this line. Note that the number N of neurons is displayed in color (black, green, purple, gray and orange) to indicate recordings from the same animal; there were a total of 5 animals.



Supplementary Figure 13: Percentage of integrated Betti values that were *not* consistent with geometric controls (i.e. above the significance threshold) across all considered data sets as a function of the correlation timescale, τ_{\max} , used to compute the pairwise correlation matrix (see Methods). The arrow indicates the 1 s timescale used in the main figures. All three behavioral conditions, spatial navigation (black), wheel running (green) and REM sleep (pink), are consistent with geometric structure at timescales ranging from .5 s to 2 s. At finer timescales, however, the wheel running and REM sleep correlations are non-geometric, while the spatial navigation data remains consistent with geometric controls.

For each timescale, we computed integrated Betti values $\bar{\beta}_1$, $\bar{\beta}_2$, and $\bar{\beta}_3$ for all data sets under three different conditions: (i) spatial navigation, (ii) wheel running, and (iii) REM sleep (see Supplementary Figure 12). For each behavioral condition, we counted how many Betti values were above the significance threshold for rejecting the geometric hypothesis at each timescale. Because our significance threshold rejects the geometric hypothesis at a rate of less than 5%, the p -value for a given condition and timescale satisfies

$$p < \sum_{\ell=k}^m \binom{m}{\ell} (0.05)^\ell (1 - 0.05)^{m-\ell},$$

where k is the number of Betti values above the significance threshold, and m is the total number of Betti values. To obtain this upper bound on p -value, we used a binomial distribution with failure probability 0.05. Note that this assumes Betti values are independent. Although this is a reasonable assumption for Betti values from different data sets, Betti values from the same data set have statistical dependencies that are not well-understood.

Supplementary Text

To accompany “Clique topology reveals intrinsic geometric structure in neural correlations.” Chad Giusti, Eva Pastalkova, Carina Curto*, and Vladimir Itskov*

Contents

1	Introduction	1
2	The order complex	3
3	Clique topology	5
3.1	The clique complex of a graph	5
3.2	Chains and boundaries	6
3.3	Homology of a clique complex	8
3.4	Clique topology across the order complex	10
3.5	Clique topology of random and geometric matrices	11
3.6	Some remarks on geometric order complexes	13
4	Computational aspects and persistence	14
4.1	A brief history of persistent homology	14
4.2	Persistent homology of order complexes	15
4.3	Persistence lifetimes of random and geometric order complexes	15
4.4	CliqueTop software	17

1 Introduction

The purpose of this supplement is to provide a more complete account of the mathematics underlying our analyses in the main text. In particular, the *order complex* and *clique topology* are described more precisely here. The order complex of a matrix is analogous to its Jordan Form, in that it captures features that are invariant under a certain type of matrix transformation. Likewise, the clique topology of a matrix is analogous to its eigenvalue spectrum, in that it provides a set of invariants that can be used to detect structure. While the Jordan Form and eigenvalue spectrum are invariant under linear change of variables, the order complex and clique topology are invariant under monotonic transformations of the matrix entries.

Seeking quantities that are invariant under linear coordinate transformations is natural in physical applications, where measurements are often performed with respect to an arbitrary basis, such as the choice of x , y and z directions in physical space. In contrast, measurements in biological settings are often obtained as nonlinear (but monotonic) transformations of the underlying “real” variables, while the choice of basis is meaningful

and fixed. For example, basis elements might represent particular neurons or genes, and measurements (matrix elements) could consist of pairwise correlations in neural activity, or the co-expression of pairs of genes. Unlike change of basis, these transformations are of the form

$$L_{ij} = f(M_{ij}),$$

where f is a nonlinear, but monotonically increasing function that is applied to each entry of M . The Jordan Form of a matrix, and its spectrum, may be badly distorted by such transformations; it also discards basis information which may be meaningful and should be preserved.

Given a symmetric, $N \times N$ matrix that reflects correlations or similarities between N entities (such as neurons, imaging voxels, etc.), we have two basic questions:

- Q1. Is the matrix a monotonic transformation of a random or geometric¹ matrix?
- Q2. Can we distinguish between these two possibilities, without knowing f ?

Perhaps surprisingly, information sufficient to answer these questions is contained in the ordering of matrix entries, and is encoded in its *order complex*, to be described in the next section. To extract the relevant features, we compute certain topological invariants of the order complex, which we refer to as the *clique topology* of the matrix. The motivation for this choice stems from recent mathematical results by M. Kahle [1], describing the clique topology of random symmetric matrices asymptotically (for large N); and our own computational results, showing that random and “generic” Euclidean distance matrices can be readily distinguished using clique topology for $N \sim 100$.

We have made an effort to keep these explanations self-contained, but details of how certain computations are performed have been left to the references for the sake of brevity. Standard material from algebraic topology [2] is described in a minimal fashion, with an emphasis on homology of clique complexes. The reader is expected to be familiar with linear algebra.

Comparison to prior applications in biology

Topological data analysis has previously been used in biological applications to identify individual persistent cycles that may have meaningful interpretation [3, 4, 5, 6, 7, 8]. In contrast, our approach relies on the *statistical properties* of cycles, as captured by Betti curves, in order to detect geometric structure (or randomness) in symmetric matrices. In particular, the relevant space from which the data points are sampled may not possess any meaningful persistent cycles, as in the square box environment covered by place fields. The background Euclidean geometry, however, has a strong effect on the statistics of cycles, enabling detection of geometric structure and providing a sharp contrast to Betti curves of random matrices with i.i.d. entries.

¹Recall from the main text that a *geometric* matrix refers to a matrix of (negative) Euclidean distances among random points in \mathbb{R}^d .

2 The order complex

Recall that a function $f : \mathbb{R} \rightarrow \mathbb{R}$ is said to be *monotonically increasing* if $f(x) > f(y)$ whenever $x > y$. Let $f : \mathbb{R} \rightarrow \mathbb{R}$ be a monotonically increasing function. For any real-valued matrix M , we define the matrix $f \cdot M$ by

$$(f \cdot M)_{ij} = f(M_{ij}).$$

Note that this action preserves the ordering of matrix entries. That is, if $L = f \cdot M$, then all pairs of off-diagonal entries, (i, j) and (k, ℓ) , satisfy:

$$L_{ij} < L_{k\ell} \Leftrightarrow M_{ij} < M_{k\ell}.$$

Equivalence classes of matrices can thus be represented by integer-valued matrices that record the ordering of off-diagonal entries (and carry no information on the diagonal). Figure 1 shows three matrix orderings for $N = 5$. For a given symmetric matrix M , we



Figure 1: Three matrix orderings, reproduced from Figure 2a in the main text.

denote the representative matrix ordering by \widehat{M} , where

$$\widehat{M}_{ij} = |\{(k, \ell) \mid 0 < k < \ell \leq N \text{ and } M_{k\ell} < M_{ij}\}|$$

simply counts the number of upper-triangular entries of M that are smaller than M_{ij} for $i \neq j$, while the diagonal entries of \widehat{M} are left undefined ($|\cdot|$ denotes the size of the set). If M_{ij} is the smallest off-diagonal entry, then $\widehat{M}_{ij} = 0$; if M_{ij} is the largest matrix entry, and all upper-triangular entries are distinct, then $\widehat{M}_{ij} = \binom{N}{2} - 1$. With this notation, we have:

Lemma 2.1. $\widehat{L} = \widehat{M}$ if and only if there exists a monotonically increasing function f such that $L = f \cdot M$.

Proof. (\Leftarrow) is obvious, since the action of f preserves the ordering of matrix entries. (\Rightarrow) One can construct $f : \mathbb{R} \rightarrow \mathbb{R}$ by setting $f(M_{ij}) = L_{ij}$ for each off-diagonal entry, and interpolating monotonically (e.g., linearly). Since we assume $\widehat{L} = \widehat{M}$, this function is monotonically increasing and well-defined. \square

In order to analyze the information present in the ordering of entries for an $N \times N$ symmetric matrix, it is useful to represent it as a sequence of nested simple graphs. Recall that a *simple graph* G is a pair $([N], E)$, where $[N] = \{1, 2, \dots, N\}$ is the ordered set of *vertices*, and E is the set of *edges*. Each edge is undirected and connects a unique pair of distinct vertices (no self-loops). We will use the notation $(ij) \in G$ to indicate that the edge corresponding to vertices i, j is in the graph.

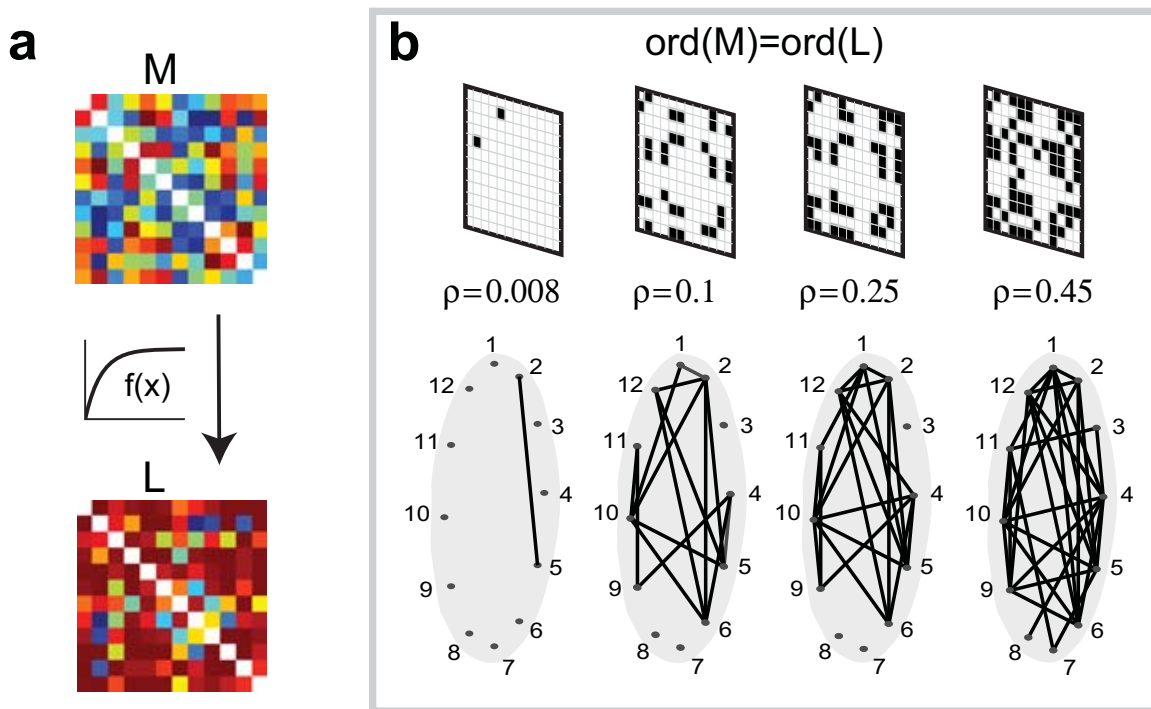


Figure 2: Selected graphs in an order complex, adapted from Figure 1 in the main text.

Definition 2.2. Let M be a real symmetric matrix with matrix ordering \widehat{M} , and let $p = \max_{i < j} \widehat{M}_{ij}$. The *order complex* of M , denoted $\text{ord}(M)$, is the sequence of graphs

$$G_0 \subset G_1 \subset \dots \subset G_{p+1},$$

such that

$$(ij) \in G_r \Leftrightarrow \widehat{M}_{ij} > p - r \text{ for each } r = 0, \dots, p + 1.$$

Note that G_0 has no edges, G_1 contains only the edge (ij) corresponding to the largest off-diagonal entry of M , and subsequent graphs are each obtained from the previous one by adding an additional edge for each next-largest entry until we reach the complete graph, G_{p+1} . A portion of an order complex is illustrated in Figure 2. It is clear from the definition that:

$$\text{ord}(L) = \text{ord}(M) \Leftrightarrow \widehat{L} = \widehat{M}.$$

Because of Lemma 2.1, the order complex $\text{ord}(M)$ captures all features of M that are preserved under the action of monotonically increasing functions.

3 Clique topology

We are now ready to introduce *clique topology*, a tool for extracting invariant features of a matrix from the ordering of matrix entries. We begin by describing the clique topology of a single graph G , by which we simply mean the homology of its *clique complex*:

$$H_i(X(G), \mathbf{k}),$$

where \mathbf{k} is a field (more on the field in section 3.2). The clique complex, $X(G)$, is defined in section 3.1; while the simplicial homology groups, $H_i(X(G), \mathbf{k})$, will be defined in section 3.3. We refer to these invariants as *clique topology* in order to indicate that we are measuring topological features of the organization of cliques in the graph, rather than the usual topology of the graph.

We summarize the information present in clique topology via a set of *Betti numbers*, $\beta_i(X(G))$, which are the ranks of the corresponding homology groups:

$$\beta_i(X(G)) \stackrel{\text{def}}{=} \text{rank } H_i(X(G), \mathbf{k}).$$

The clique topology of a symmetric matrix M , with order complex $G_0 \subset G_1 \subset \dots \subset G_{p+1}$, is reflected in the sequences of Betti numbers $\beta_i(X(G_r))$, computed for various dimensions $i = 0, 1, 2, \dots$, and for each graph G_r in $\text{ord}(M)$ (see section 3.4).

The reader familiar with homology of simplicial complexes, including clique complexes, should feel free to skip the next few sections and proceed directly to section 3.4, where we define *Betti curves*.

3.1 The clique complex of a graph

Recall that a *clique* in a graph G is an all-to-all connected collection of vertices in G . An *m-clique* is a clique consisting of m vertices. Note that if σ is a clique of G , then all subsets of σ are also cliques.

Definition 3.1. Let G be a graph with N vertices. The *clique complex* of G , denoted $X(G)$, is the set of all cliques of G :

$$X(G) = \{\sigma \subset [N] \mid \sigma \text{ is a clique of } G\}.$$

We write $X_m(G)$ for the set of $(m + 1)$ -cliques of G .

The shift in index reflects the “dimension” of a clique, when the clique complex is represented geometrically. If we think of the vertices of the graph G as embedded generically in a high-dimensional space, each clique represents the simplex given by the convex hull of its vertices. For example, the convex hull of two vertices is a 1-dimensional edge, for three vertices we obtain a 2-dimensional triangle, and four vertices yields a 3-dimensional tetrahedron. Thus, cliques in $X_m(G)$ consist of $m + 1$ vertices, but represent m -dimensional simplices.

The *boundary* of a clique $\sigma \subseteq G$ is the collection of subcliques $\tau \subset \sigma$ which have one fewer vertex. This corresponds to the set of lower-dimensional simplices that comprise the boundary of the simplex defined by σ (Figure 3b).

The *homology* of a clique complex $X(G)$, to be defined in section 3.3, is a measurement of relationships among the cliques in G . Intuitively, homology counts *cycles* in the clique complex, a higher-dimensional generalization of the notion of cycles in a graph (Figure 3a). A collection of cliques forms a cycle if their boundaries overlap so as to “cancel” one another (Figure 3b).

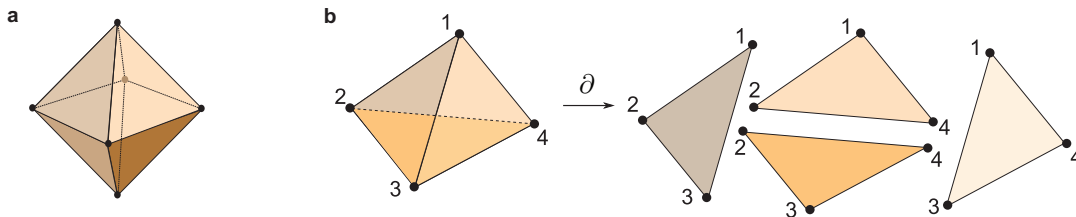


Figure 3: Illustration of homology cycles in clique complexes.

3.2 Chains and boundaries

To make the above notion of “cancellation” of boundaries precise (and computable), one introduces linear combinations of cliques, called *chains*. Given a set of cliques $\sigma_1, \dots, \sigma_\ell \in X(G)$, one can form a vector space consisting of formal linear combinations of cliques with coefficients in a field \mathbf{k} :

$$\sum_{i=1}^{\ell} a_i c_{\sigma_i}, \quad \text{where } a_i \in \mathbf{k},$$

and c_{σ_i} denotes the basis element corresponding to the clique σ_i . To define chain groups, one considers linear combinations of cliques of the same size. Recall that $X_m(G)$ denotes the set of $(m + 1)$ -cliques of G .

Definition 3.2. The m -th chain group of $X(G)$, with coefficients in \mathbf{k} , is the \mathbf{k} -vector

space:

$$C_m(X(G); \mathbf{k}) \stackrel{\text{def}}{=} \left\{ \sum_{i=1}^{\ell} a_i c_{\sigma_i} \mid \sigma_i \in X_m(G) \text{ and } a_i \in \mathbf{k} \text{ for each } i = 1, \dots, \ell \right\}.$$

As we will always be working with coefficients in an arbitrary field \mathbf{k} ,² we will omit it from the notation and write $C_m(X(G))$ instead of $C_m(X(G); \mathbf{k})$. Note that $C_0(X(G))$ consists of formal linear combinations of 1-cliques (vertices), $C_1(X(G))$ of 2-cliques (edges), $C_2(X(G))$ of 3-cliques (triangles), and so on.

The boundaries of cliques can also be described algebraically, allowing this notion to be extended to chains. If $\sigma = \{v_i\}_{i=0}^m$ is an m -clique of G , we use the notation

$$c_\sigma = c_{v_0 v_1 \dots v_m},$$

where $v_0 < v_1 < \dots < v_m$ (recall that each $v_i \in [N]$). Consistent ordering is important because it affects the signs in the boundary map. Given a sequence of vertices $v_0 v_1 \dots v_m$, we denote by $v_0 v_1 \dots \hat{v}_i \dots v_m$ the sequence obtained by omitting the element v_i . Note that for each $\sigma \in X_m(G)$, the element $c_\sigma = c_{v_0 v_1 \dots v_m}$ is a basis element of the vector space $C_m(X(G))$.

Definition 3.3. The *boundary* map $\partial_m : C_m(X(G)) \rightarrow C_{m-1}(X(G))$, for $m > 0$, is given on basis elements $c_{v_0 v_1 \dots v_m}$ by

$$\partial_m(c_{v_0 v_1 \dots v_m}) = \sum_{i=0}^m (-1)^i c_{v_0 v_1 \dots \hat{v}_i \dots v_m},$$

and is extended via linearity to general chains; i.e. $\partial_m(\sum_j a_j c_{\sigma_j}) = \sum a_j \partial_m(c_{\sigma_j})$. The map ∂_0 is defined to be the zero map.

Recall that in the geometric picture, an $(m+1)$ -clique corresponds to a m -dimensional simplex, and the boundary of this simplex is the set of m -cliques comprising its $(m-1)$ -dimensional *facets* – that is, all subcliques on one fewer vertex. We have thus defined the boundary of a chain in $C_m(X(G))$ in a fashion consistent with our geometric understanding: as a formal sum of chains in $C_{m-1}(X(G))$, corresponding to simplices that are one dimension lower (see Figure 3b). Note that signs are assigned to the elements of this formal sum to indicate the *orientation* of cliques, which will be critical for obtaining the desired “cancellation” of boundaries (see Remark 3.6 for details).

²For readers uncomfortable with the notion of a general field \mathbf{k} , it is relatively harmless to substitute \mathbb{R} or \mathbb{Q} for \mathbf{k} for the remainder of the discussion. One should keep in mind, however, that the actual computations typically take place with \mathbf{k} a finite field, $\mathbb{Z}/p\mathbb{Z}$. This can have an effect on the result: in such a field, one can add a boundary to itself a finite number of times and get zero, creating “extra” cycles – called *torsion* cycles – that would not be present over \mathbb{R} . These extra cycles measure aspects of the clique complex that are not relevant to our purposes. In our software we have chosen the field to be $\mathbb{Z}/2\mathbb{Z}$, but this choice is somewhat arbitrary and not important. So long as all computations are done using the same field, comparing the resulting homology groups across different graphs is entirely valid.

Example 3.4. Suppose $\sigma, \tau \in X_2(G)$ are cliques on vertices $\{1, 2, 3\}$ and $\{1, 2, 4\}$ respectively. The boundary of the 2-chain $c_\sigma - c_\tau \in C_2(X(G))$ is

$$\begin{aligned} \partial_2(c_{123} - c_{124}) &= \partial_2(c_{123}) - \partial_2(c_{124}) \\ &= (c_{23} - c_{13} + c_{12}) - (c_{24} - c_{14} + c_{12}) \\ &= c_{23} - c_{13} - c_{24} + c_{14}. \end{aligned}$$

The cancellation of c_{12} reflects the fact that the clique $\{1, 2\}$ appears twice in the boundary of $c_\sigma - c_\tau$, with *opposite* orientation. Note also that applying ∂_1 to the resulting 1-chain yields

$$\begin{aligned} \partial_1(\partial_2(c_{123} - c_{124})) &= \partial_1(c_{23} - c_{13} - c_{24} + c_{14}) \\ &= (c_3 - c_2) - (c_3 - c_1) - (c_4 - c_2) + (c_4 - c_1) \\ &= 0. \end{aligned}$$

In fact, it is straightforward to check from the definition that the composition of two subsequent boundary maps always yields 0. In other words,

Lemma 3.5. *For any $m > 0$, $\partial_m \circ \partial_{m+1} = 0$.*

Remark 3.6. The *orientation* of cliques can be *positive* or *negative*. The vertices of a clique $c_{v_0 v_1 \dots v_m} \in X_m(G)$ have a *canonical* ordering induced by the usual ordering of the vertices $[N]$ of G . We define the canonical ordering to have positive orientation for each clique. Any other ordering can be obtained as a permutation of the canonical ordering, and the resulting ordering is positive or negative according to the sign of the permutation. For example, c_{124} has a positive orientation, while c_{214} is negatively oriented. When we compute the boundary of a clique c_σ in Definition 3.3, the signs arise as a result of the *induced orientation* on the boundary cliques. The result of taking all cliques on the boundary is the signed sum we obtain in Definition 3.3.

3.3 Homology of a clique complex

For a given graph G , the chain groups $C_m(X(G))$ can be strung together to form a *chain complex*:

$$0 \xrightarrow{\partial_{k+1}=0} C_k(X(G)) \xrightarrow{\partial_k} C_{k-1}(X(G)) \xrightarrow{\partial_{k-1}} \dots \xrightarrow{\partial_2} C_1(X(G)) \xrightarrow{\partial_1} C_0(X(G)) \xrightarrow{\partial_0=0} 0,$$

The zeroes at either end of the complex represent the zero-dimensional \mathbf{k} -vector space, and the maps at each end are necessarily the zero map.

If a chain is in the kernel of the boundary map, it is because the (oriented) boundaries of its constituent cliques cancel one another. This is precisely the desired notion of a *cycle*, so the set of m -cycles is exactly $\ker(\partial_m)$; in particular, 1-cycles correspond to the

usual notion of cycles in a graph. Note also that any chain in $C_m(X(G))$ which forms the boundary of a clique in $X_{m+1}(G)$ is itself a cycle, so its own boundary should be zero. This is reflected in the fact that $\partial_m \circ \partial_{m+1} = 0$ (Lemma 3.5). In particular,

$$\text{im } \partial_{m+1} \subset \ker \partial_m.$$

When we are counting cycles for homology, we do not want to consider those which arise as boundaries of chains, as these are “filled in.” For example, the two clique complexes in Figure 4 should have the same number of homology 1-cycles. In Figure 4b, we do not wish to count the chain $c_{23} + c_{35} - c_{25} \in C_1(X(G))$ as a 1-cycle because it is the boundary of a clique, $c_{235} \in C_2(X(G))$.

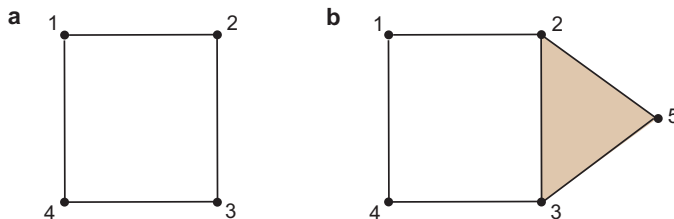


Figure 4: Two clique complexes for graphs on 4 and 5 vertices.

In order to eliminate cycles that are boundaries of higher-dimensional cliques, one computes quotient vector spaces, $\ker(\partial_m)/\text{im}(\partial_{m+1})$.

Definition 3.7. The m -th homology group of $X(G)$ with coefficients in \mathbf{k} is the quotient space

$$H_m(X(G); \mathbf{k}) \stackrel{\text{def}}{=} \frac{\ker(\partial_m)}{\text{im}(\partial_{m+1})}.$$

As with chain groups, we will omit the field from our notation and write simply $H_m(X(G))$.

Observe that the zeroth homology group is special: since $\partial_0 = 0$, its kernel is always $C_0(X(G))$. The quotient $\ker(\partial_0)/\text{im}(\partial_1)$ thus identifies vertices which are connected to one another, so that $H_0(X(G))$ is a vector space whose basis can be chosen to correspond to the *connected components* of G .

Example 3.8. Let G be the graph on four vertices in Figure 4a. The kernel of the boundary map $\partial_1 : C_1(X(G)) \rightarrow C_0(X(G))$ is the one-dimensional space spanned by $\sigma = c_{12} + c_{23} + c_{34} - c_{14}$. Indeed, $\partial_1(\sigma) = (c_2 - c_1) + (c_3 - c_2) + (c_4 - c_3) - (c_4 - c_1) = 0$. Since there are no cliques of size greater than 2, $C_2(X(G)) = 0$ and hence $\partial_2 = 0$. It follows that $H_1(X(G))$ is precisely the one-dimensional vector space spanned by σ . Furthermore, since $C_1(X(G))$ has dimension 4 and $\ker \partial_1$ has dimension 1, it follows that $\text{im } \partial_1$ has dimension 3. We can thus deduce that $H_0(X(G))$ is also one-dimensional, consistent with the fact that G has just one connected component.

Next, consider the graph G' on five vertices in Figure 4b. This graph has been obtained from G by “attaching” the clique $\{2, 3, 5\}$. The kernel of ∂_1 is now 2-dimensional, and is spanned by both σ and a new cycle, $\tau = c_{23} + c_{35} - c_{25}$. However, $\tau \in \text{im } \partial_2$, so we find that $H_1(X(G'))$ continues to be one-dimensional, consistent with our intuition that G and G' both have just one cycle that has not been “filled in” by cliques.

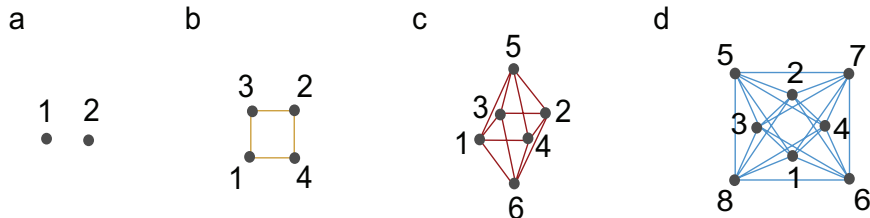


Figure 5: Cross-polytopes generate the minimal clique complexes which produce homology in each dimension. Adapted from Figure 1 of the main text.

Example 3.9. The smallest example of a graph G_m whose clique complex has non-trivial m -th homology group is the 1-skeleton of the $(m + 1)$ -dimensional cross-polytope (Figure 5). Such a graph can be built inductively starting from the graph G_0 (Figure 5a), having just two vertices and no edges. To obtain G_1 from G_0 , we attach two new vertices and include all edges between the new vertices and the vertices of G_0 (Figure 5b). More generally, to obtain G_i from G_{i-1} we attach two new vertices and all edges between these new vertices and those of G_{i-1} . Thus, we obtain G_2 (Figure 5c) and G_3 (Figure 5d), which give minimal examples of graphs whose clique complexes have a non-trivial homology 2-cycle and 3-cycle, respectively.

A useful characterization of the clique topology of a graph is obtained by simply tracking the dimensions of the homology groups. This is done via the so-called Betti numbers.

Definition 3.10. The m -th Betti number of $X(G)$, denoted $\beta_m(X(G))$, is the rank of $H_m(X(G); \mathbf{k})$ as a \mathbf{k} -vector space.

While this information discards the identities of individual cycles, it is well-suited to statistical methods as it reduces the clique topology of a graph to a sequence of integers.

3.4 Clique topology across the order complex

We now turn our attention to the clique topology of all graphs in the order complex at once. For a matrix M , the Betti numbers of the graphs in $\text{ord}(M)$ are collected as follows.

Definition 3.11. Let M be a real symmetric matrix and $\text{ord}(M) = (G_0 \subset G_1 \subset G_2 \subset \dots \subset G_{p+1})$ its order complex, where $p = \max_{i < j} \widehat{M}_{ij}$. The m -th Betti curve of M is the

sequence of numbers $\{\beta_m(\rho_r)\}_{r=1}^{p+1}$, where ρ_r is the edge density of the graph G_r , and

$$\beta_m(\rho_r) \stackrel{\text{def}}{=} \text{rank } H_m(X(G_r)).$$

As the matrix M will be clear from context, we omit it from the notation.

While each Betti curve is a discrete sequence, we can think of it as being a piecewise constant function. To simplify comparison, we consider as a summary statistic the integral of the entire Betti curve. We call this the *m-th total Betti number* of the matrix M , given by

$$\bar{\beta}_m(M) \stackrel{\text{def}}{=} \sum_{r=1}^{p+1} \beta_m(\rho_r) \Delta\rho_r = \int_0^1 \beta_m(\rho) \, d\rho,$$

where $\Delta\rho_r$ is the change in edge density between G_r and G_{r-1} .³ Typically, $\Delta\rho_r = 1/\binom{N}{2}$, which is the change in density after adding a single edge. As we will see, the $\bar{\beta}_m$ alone can distinguish between a random symmetric matrix, drawn from a distribution with i.i.d. entries, and a geometric matrix, which arises from distances between a set of randomly-distributed points in Euclidean space. Thus, we can use the total Betti number to test the hypotheses that a matrix is random or geometric.

3.5 Clique topology of random and geometric matrices

In order to interpret the results of computing clique topology for matrices of interest, we need suitable null models for comparison. This brings us back to our motivating questions Q1 and Q2 from section 1. Can we use clique topology to reject the hypothesis that a given matrix is random or geometric? This will be possible if matrices in these categories have stereotyped Betti curves. In this case, it can be shown that a matrix with a substantially different Betti curve is unlikely to have come from the given null model distribution, and a *p*-value can be assigned to quantify the significance.

Because clique topology depends only on $\text{ord}(M)$, it suffices to describe the distributions of order complexes we obtain for random and geometric matrices. In both families, the details of the Betti curves change with N ; however, we find that their large-scale features are robust once $N > 50$. This means Betti curves can indeed be used to reject these models.

The distribution of *random order complexes* arises by sampling a matrix ordering \widehat{M} from the uniform distribution on all such orderings. For $N \times N$ symmetric matrices with distinct entries $\{M_{ij}\}_{i < j}$, this can be achieved by sampling permutations of $\{0, \dots, \binom{N}{2} - 1\}$ uniformly at random. Equivalently, the matrix can be chosen with i.i.d. entries drawn from any continuous distribution, or by shuffling the elements of a given matrix with

³This measurement, $\bar{\beta}_m(M)$, also appears as the first element in the basis for the ring of algebraic functions on the collection of all persistence structures described in [9].

distinct off-diagonal entries. Thus, in a graph G_ρ of $\text{ord}(M)$, each edge has independent probability ρ of appearing. In other words, the graphs in the order complex are a nested family of Erdős-Rényi random graphs. The clique topology of such complexes is relatively well understood from a theoretical perspective [1], with highly stereotyped, unimodal Betti curves as illustrated in Figure 6a.

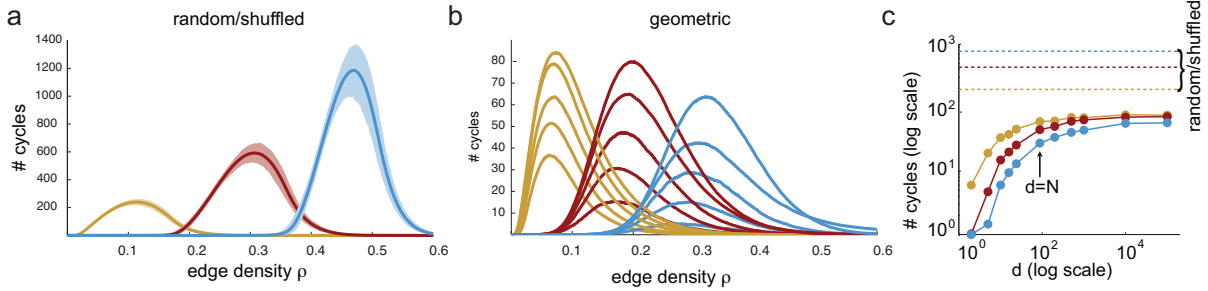


Figure 6: Betti curves for random and geometric matrices. **(a)** Betti curves of random matrices with $N = 100$. The means for the Betti curves $\beta_1(\rho)$ (yellow), $\beta_2(\rho)$ (red), and $\beta_3(\rho)$ (blue) are displayed with bold lines, while shading indicates 99.5% confidence intervals. **(b)** Betti curves of geometric matrices with $N = 100$. Average Betti curves are displayed for dimensions $d = 10, 50, 100, 1000, 10000$, in increasing order (i.e., higher curves correspond to larger dimensions). **(c)** The maxima of Betti curves for $N = 88$ geometric matrices as a function of dimension. Beyond $d = N$, peak values increase only slightly and appear to saturate. The $d = 10^4$ and $d = 10^5$ values are nearly identical, and far from the peak values for random/shuffled matrices with matching N (dashed lines). Adapted from Figure 2b of the main text.

A *geometric order complex* is one arising from the negative distance matrix of a collection of points embedded in some Euclidean space. We choose *negative* distance matrices so that the highest matrix values correspond to the nearest distances; this is consistent with the intuition that correlations should decrease with distance, as described in the main text. Sampling such a complex consists of sampling N i.i.d. points, $\{p_i\}$, from some distribution on \mathbb{R}^d . The associated sequence of clique complexes, $X(G_0) \subset X(G_1) \subset \dots \subset X(G_{p+1})$, corresponding to a geometric order complex is also referred to as the *Vietoris-Rips complex* of the underlying points. These complexes have been heavily studied in cases where the points are presumably sampled from an underlying manifold [10].

In our setting, we sample points from the uniform distribution on the unit cube in \mathbb{R}^d . To our knowledge, the Betti curves of geometric order complexes are largely unstudied. Our numerical experiments show that they are highly stereotyped (Figure 6b), irrespective of d for a large range of dimensions. Moreover, the peaks of the geometric Betti curves are roughly an order of magnitude smaller than those of random order complexes with matching N , and the peak values *decrease* rather than increase as we move between $\beta_1(\rho)$

to $\beta_2(\rho)$ and $\beta_3(\rho)$. We observed similar Betti curves to those in Figure 6b for values of d that were orders of magnitude larger than N , testing dimensions up to $d = 10^5$ (for $N = 88$). Beyond $d = N$, peak values of Betti curves increase only slightly and appear to saturate, while remaining far from random/shuffled Betti curves (Figure 6c). The differences between the Betti curves of random and geometric matrices can also be understood through the lens of *persistence lifetimes*, which we will describe in section 4.2.

3.6 Some remarks on geometric order complexes

Any matrix ordering \widehat{M} appears with equal probability in the distribution of random symmetric matrices with i.i.d. entries. The consistency of the Betti curves in Figure 6a indicates that “most” of these matrix orderings have a similar organization of cliques. For geometric matrices, the possible matrix orderings are sampled in a highly non-uniform manner, leading to dramatically different Betti curves. Despite this, it is worth noting that any matrix ordering can in fact arise from a geometric matrix.

Definition 3.12. A set of points $p_1, \dots, p_N \in \mathbb{R}^d$ is called a *geometric realization* of the matrix ordering \widehat{M} if the distance matrix $D_{ij} = \|p_i - p_j\|$ has $\widehat{D} = \widehat{M}$.

Note that for each collection of three or more points, the (higher) triangle inequalities implied by the metric impose strong constraints on \widehat{M} . This means that for most matrix orderings, the probability of sampling a point configuration in the unit cube that yields a geometric realization of \widehat{M} is vanishingly small. This is why geometric Betti curves are, on average, so different from those of random matrices. Nevertheless, geometric realizations do always exist, provided $d \geq N - 1$.

Lemma 3.13. Every $N \times N$ matrix ordering \widehat{M} that has $\binom{N}{2}$ distinct off-diagonal entries possesses a geometric realization in $(N - 1)$ -dimensional Euclidean space. Moreover, this realization can be chosen as

$$p_i = \frac{1}{\sqrt{2}} \left(\vec{e}_i - \frac{\varepsilon}{2} \sum_{j=1}^N M_{ij} \vec{e}_j \right),$$

for small enough $\varepsilon > 0$, where M is any symmetric matrix with ordering \widehat{M} and zeroes on the diagonal, and $\{\vec{e}_i\}_{i=1}^N$ is the standard orthonormal basis in \mathbb{R}^N .

Proof. With the choice above, $\|p_i - p_j\|^2 = \|p_i\|^2 + \|p_j\|^2 - 2p_i \cdot p_j = 1 + \varepsilon M_{ij} + \mathcal{O}(\varepsilon^2)$. \square

Despite this fact, when we constrain the dimension d of the Euclidean space we do find matrix orderings that cannot be geometrically realized at all. This was the basis for our examples in Figure 2a of the main text.

Figure 2a examples from the main text. Here we prove that the $d \geq 2$ and $d \geq 3$ matrices (reproduced in Figure 1) cannot be geometrically realized in lower dimensions.

To see why the $d \geq 2$ matrix cannot arise from an arrangement of points on a line, observe that the three smallest matrix entries are M_{12}, M_{13} , and M_{14} . This implies the three shortest distances in a corresponding point arrangement must all involve the point p_1 , which is not possible for points on a line.

To see why the $d \geq 3$ matrix cannot arise from an arrangement of points on a plane, notice that the six smallest matrix entries are $M_{i\alpha}$, for $i = 1, 2, 3$ and $\alpha = 4, 5$. This means the six smallest distances are those of the form $\|p_i - p_\alpha\|$, for $i = 1, 2, 3$ and $\alpha = 4, 5$. Without loss of generality we can assume $\|p_i - p_\alpha\| < 1$, and all other distances are greater than one. Now suppose the points p_1, \dots, p_5 all lie in a plane. Then $p_4, p_5 \in D(p_1) \cap D(p_2) \cap D(p_3)$, where $D(p_i)$ is a disk of radius 1 centered at p_i . Since none of the disk centers is contained in any of the other two disks, the largest distance between two points in the intersection $D(p_1) \cap D(p_2) \cap D(p_3)$ is less than one, and thus $\|p_4 - p_5\| < 1$, which is a contradiction. We conclude that the matrix cannot arise from points in the plane. We thank Anton Petrunin for this example.

4 Computational aspects and persistence

Each graph in an order complex, $G_0 \subset G_1 \subset \dots \subset G_{p+1}$, is a subgraph of its successor. Intuitively, this means that the clique topology of any G_r is closely related to the clique topology of the previous graph, G_{r-1} . Exploiting this structure dramatically reduces the computational complexity of finding Betti curves (defined in section 3.4), and also provides us with finer matrix invariants in the form of *persistence lifetimes* of cycles. This is achieved via *persistent homology*, an approach that enables homology cycles to be tracked as we move from one graph in the order complex to the next.

4.1 A brief history of persistent homology

The mathematics underlying persistent homology has existed since the middle of the twentieth century, in the guise of Morse theory and spectral sequences for the homology of filtered spaces. Its interpretation as a tool for data analysis, however, is a much more recent development. One can trace the origins of these applications to work on size theory in computer vision [11, 12, 13] and alpha shapes in computational geometry [14, 15, 16, 17]. The use of persistent homology as a tool for the study of data sets relies on two fundamental and recent developments: computability and robustness.

Computability arose from the *persistence algorithm*, developed first for subsets of three-dimensional complexes in [17] and then extended to work with general simplicial complexes in [18]. In addition to the algorithm, these papers introduced the notions of persistence diagrams and modules. Several software packages [19, 20, 21] have been developed based on the persistence algorithm, and recent work using discrete Morse theory has led to further improvements in speed and memory efficiency [22].

Robustness to perturbations of the underlying simplicial complexes, on the other hand, was first explicitly shown through the bottleneck stability theorem of [23]. Further work has broadened this result by developing more complete theoretical tools for the comparison of persistence structures, divorcing their stability from any underlying geometry [24, 25, 26]. It is this interpretation of stability that most clearly applies to our study of order complexes.

Although persistent homology has only recently emerged a tool for studying features of data, it has already found a broad range of applications [27, 28, 29, 30].

4.2 Persistent homology of order complexes

Here we present the basic ideas in persistent homology, restricted to the special case of computing clique topology for order complexes. This means we need to apply the persistence algorithm to filtered families of clique complexes,

$$X(G_0) \subset X(G_1) \subset \cdots \subset X(G_p) \subset X(G_{p+1}),$$

where the graphs $\{G_r\}$ comprise the order complex of a symmetric matrix. In order to track homology cycles from one clique complex to the next, we need to understand how the natural inclusion maps on the graphs, $\iota_r : G_r \hookrightarrow G_{r+1}$, translate to maps on the corresponding cliques, chains, and homology groups, $H_m(X(G_r))$. This turns out to be straightforward, as there is an obvious extension to maps on clique complexes, $\iota_r : X(G_r) \hookrightarrow X(G_{r+1})$, and these in turn can be extended linearly to maps between chain groups.

Lemma 4.1. *Consider the order complex $G_0 \subset G_1 \subset \cdots \subset G_{p+1}$. The standard inclusion maps, $\iota_r : G_r \hookrightarrow G_{r+1}$, induce maps on homology $(\iota_r)_m : H_m(X(G_r)) \rightarrow H_m(X(G_{r+1}))$.*

Using these maps, one can follow individual cycles and understand their evolution as we move from one graph to the next in the order complex. Of particular interest are the edge densities at which cycles appear and disappear (Figure 7).

Definition 4.2. Let $\omega \in H_m(X(G_r))$ be a non-zero cycle which is not in the image of ι_{r-1} , and let $s > r$ be the smallest integer such that $\iota_{s-1} \circ \iota_{s-2} \circ \cdots \circ \iota_r(\omega) = 0$. We say that ω is *born* at r and *dies* at s , and has *persistence lifetime* $\ell(\omega) = s - r$.

For a given order complex, the distribution of persistence lifetimes provides a measure of matrix structure that is complementary to the Betti curves defined in section 3.4.

4.3 Persistence lifetimes of random and geometric order complexes

Recall that there is a sharp qualitative difference in the Betti curves of random order complexes and those of geometric order complexes (Figure 6). These differences are also

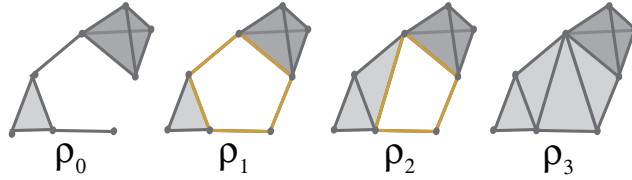


Figure 7: Illustration of persistence lifetime. The 1-cycle (yellow) appears at edge density ρ_1 and disappears at ρ_3 , so its lifetime is $\ell = \rho_3 - \rho_1$.

reflected in the distributions of their persistence lifetimes. While random complexes have relatively broad distributions (Figure 8a), the geometric complexes are heavily weighted toward shorter lifetimes (Figure 8b). The shapes of these distributions are a direct consequence of the order in which edges are added in the order complex.

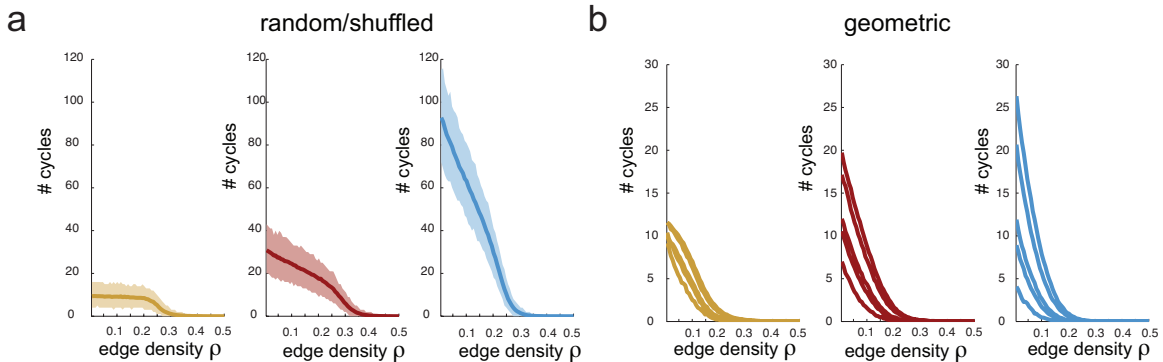


Figure 8: Persistence lifetimes for random and geometric matrices. (a) $N = 100$, and mean lifetime distributions for 1-cycles (yellow), 2-cycles (red), and 3-cycles (blue) are displayed with bold lines, while shading indicates 99.5% confidence intervals. (b) $N=100$, and average lifetime distributions are displayed for dimensions $d = 10, 50, 100, 1000, 10000$, in increasing order (i.e., higher curves correspond to larger dimensions).

The qualitative differences in these distributions can be understood by thinking about dependencies in edge orderings in the order complex. Minimal cycles, represented by cross-polytopes (Figure 5), are known to constitute the large majority of cycles in random order complexes [31], and can thus be used to understand the shape of the distribution. Such a cycle's lifetime is governed by the density at which the first additional edge appears, since the extra edge destroys the cycle by creating new cliques. Since the ordering of the edges is completely random, the lifetimes will be broadly distributed. In contrast, geometric order complexes are constrained by triangle inequalities (and higher-dimensional

analogues); these produce dependencies in the edge ordering which imposes an upper limit on the lifetime of small cycles, like the cross-polytopes.⁴ Persistence lifetimes in geometric complexes are thus concentrated at short lifetimes.

4.4 CliqueTop software

To compute clique topology for symmetric matrices, we developed the CliqueTop Matlab package. This software is maintained by Chad Giusti (one of the authors), and is available on GitHub at <https://github.com/nebneuron/cliq-top>. At the time of this writing, CliqueTop makes use of one other package: Perseus [22], by Vidit Nanda. Perseus provides an implementation of the persistence algorithm, and is available at <http://www.sas.upenn.edu/~vnanda/perseus/index.html>. Previous versions of CliqueTop also used the Cliquer software package [32].

References

- [1] Matthew Kahle. Topology of random clique complexes. *Discrete Math.*, 309(6):1658–1671, 2009.
- [2] Allen Hatcher. *Algebraic topology*. Cambridge University Press, Cambridge, 2002.
- [3] Carina Curto and Vladimir Itskov. Cell groups reveal structure of stimulus space. *PLoS Comput Biol*, 4(10), 2008.
- [4] Gurjeet Singh, Facundo Memoli, Tigran Ishkhanov, Guillermo Sapiro, Gunnar Carlsson, and Dario L Ringach. Topological analysis of population activity in visual cortex. *Journal of vision*, 8(8):11, 2008.
- [5] Monica Nicolau, Arnold J. Levine, and Gunnar Carlsson. Topology based data analysis identifies a subgroup of breast cancers with a unique mutational profile and excellent survival. *Proceedings of the National Academy of Sciences*, 108(17):7265–7270, 2011.
- [6] Y. Dabaghian, F. Memoli, L. Frank, and G. Carlsson. A topological paradigm for hippocampal spatial map formation using persistent homology. *PLoS Comput Biol*, 8(8), 08 2012.
- [7] Joseph Minhow Chan, Gunnar Carlsson, and Raul Rabadan. Topology of viral evolution. *Proceedings of the National Academy of Sciences*, 2013.

⁴This is true statistically. It is, of course, possible for two distances to be close in absolute terms and still be separated by many edges in the order complex, but this is rare enough that the intuition about Betti curves still holds.

- [8] Zhe Chen, Stephen N. Gomperts, Jun Yamamoto, and Matthew A. Wilson. Neural representation of spatial topology in the rodent hippocampus. *Neural computation*, 26(1):1–39, Jan 2014.
- [9] Aaron Adcock, Erik Carlsson, and Gunnar Carlsson. The ring of algebraic functions on persistence bar codes, 2013.
- [10] Anne D. Collins, Afra Zomorodian, Gunnar E. Carlsson, and Leonidas J. Guibas. A barcode shape descriptor for curve point cloud data. *Computers & Graphics*, 28(6):881–894, 2004.
- [11] Patrizio Frosini and Claudia Landi. Persistent Betti numbers for a noise tolerant shape-based approach to image retrieval. In *Computer analysis of images and patterns. Part I*, volume 6854 of *Lecture Notes in Comput. Sci.*, pages 294–301. Springer, Heidelberg, 2011.
- [12] Francesca Cagliari, Massimo Ferri, and Paola Pozzi. Size functions from a categorical viewpoint. *Acta Appl. Math.*, 67(3):225–235, 2001.
- [13] Patrizio Frosini and Michele Mulazzani. Size homotopy groups for computation of natural size distances. *Bull. Belg. Math. Soc. Simon Stevin*, 6(3):455–464, 1999.
- [14] V. Robins. Towards computing homology from finite approximations. In *Proceedings of the 14th Summer Conference on General Topology and its Applications (Brookville, NY, 1999)*, volume 24, pages 503–532 (2001), 1999.
- [15] H. Edelsbrunner. The union of balls and its dual shape. *Discrete Comput. Geom.*, 13(3-4):415–440, 1995.
- [16] H. Edelsbrunner and E. P. Mucke. Three-dimensional alpha shapes. *ACM Trans. Graphics*, 13:43–72, 1994.
- [17] Herbert Edelsbrunner, David Letscher, and Afra Zomorodian. Topological persistence and simplification. In *41st Annual Symposium on Foundations of Computer Science (Redondo Beach, CA, 2000)*, pages 454–463. IEEE Comput. Soc. Press, Los Alamitos, CA, 2000.
- [18] Afra Zomorodian and Gunnar Carlsson. Computing persistent homology. *Discrete Comput. Geom.*, 33(2):249–274, 2005.
- [19] Andrew Tausz, Mikael Vejdemo-Johansson, and Henry Adams. Javaplex: A research software package for persistent (co)homology. <http://javaplex.github.io/javaplex/>, 2011.

- [20] Dmitriy Morozov. Dionysis, c++ library for computing persistent homology. <http://www.mrzv.org/software/dionysus/>, 2011–2014.
- [21] Andrew Tausz. phom: Persistent homology in r. <http://cran.r-project.org>, 2011.
- [22] Vidit Nanda. Perseus, the persistent homology software. <http://www.sas.upenn.edu/~vnanda/perseus> Accessed 06/14, 2012–2014.
- [23] David Cohen-Steiner, Herbert Edelsbrunner, and John Harer. Stability of persistence diagrams. *Discrete Comput. Geom.*, 37(1):103–120, 2007.
- [24] F. Chazal, D. Cohen-Steiner, M. Glisse, L. J. Guibas, and S. Y. Oudot. Proximity of persistence modules and their diagrams. In *Proc. 25th Annu. Symposium on Computational Geometry*, pages 237–246, 2009.
- [25] Frederic Chazal, Vin de Silva, Marc Glisse, and Steve Oudot. The structure and stability of persistence modules, 2012.
- [26] Frederic Chazal, Vin de Silva, and Steve Oudot. Persistence stability for geometric complexes, 2012.
- [27] Joseph Minhow Chan, Gunnar Carlsson, and Raul Rabadan. Topology of viral evolution. *Proc. Natl. Acad. Sci. USA*, 110(46):18566–18571, 2013.
- [28] Gurjeet Singh, Facundo Memoli, Tigran Ishkhanov, Guillermo Sapiro, Gunnar Carlsson, and Dario L Ringach. Topological analysis of population activity in visual cortex. *Journal of vision*, 8(8):11, 2008.
- [29] Jennifer Gamble and Giseon Heo. Exploring uses of persistent homology for statistical analysis of landmark-based shape data. *Journal of Multivariate Analysis*, 101(9):2184 – 2199, 2010.
- [30] Gunnar Carlsson, Tigran Ishkhanov, Vin de Silva, and Afra Zomorodian. On the local behavior of spaces of natural images. *Int. J. Comput. Vision*, 76(1):1–12, January 2008.
- [31] Matthew Kahle and Elizabeth Meckes. Limit theorems for Betti numbers of random simplicial complexes. *Homology Homotopy Appl.*, 15(1):343–374, 2013.
- [32] Sampo Niskanen and Patric Östergård. Cliquer. <http://users.tkk.fi/pat/cliquer.html>, 2002.